

FIRST RESULTS FROM THE NOAO SURVEY OF THE OUTER LIMITS OF THE MAGELLANIC CLOUDS

ABHIJIT SAHA^{1,10,11}, EDWARD W. OLSZEWSKI^{2,11}, BRIAN BRONDEL^{3,11,12}, KNUT OLSEN^{1,10,11}, PATRICIA KNEZEK^{1,10,11}, JASON HARRIS^{1,10,11}, CHRIS SMITH⁴, ANNAPURNI SUBRAMANIAM^{5,11}, JENNIFER CLAVER¹, ARMIN REST^{4,13,14}, PATRICK SEITZER⁶, KEM H. COOK⁷, DANTE MINNITI^{8,15}, AND NICHOLAS B. SUNTZEFF⁹

¹ National Optical Astronomy Observatory, Tucson, AZ 85719, USA; saha@noao.edu, kolsen@noao.edu, pknezek@noao.edu, jharris@30doradus.org, jlclaver@noao.edu

² Steward Observatory, The University of Arizona, Tucson, AZ, USA; eolszewski@as.arizona.edu

³ Department of Astronomy, Indiana University, Swain West 319, 727 East Third Street, Bloomington, IN 47405-7105, USA; bbrondel@gmail.com

⁴ Cerro Tololo Inter-American Observatory, National Optical Astronomy Observatory, Casilla 603, La Serena, Chile; csmith@ctio.noao.edu, rest@ctio.noao.edu

⁵ Indian Institute of Astrophysics, Koramangala II Block, Bangalore 34, India; purni@iiap.res.in

⁶ Department of Astronomy, University of Michigan, Ann Arbor, MI 48109, USA; pseitzer@umich.edu

⁷ IGPP, Lawrence Livermore National Laboratory, MS L-413, P.O. Box 808, Livermore, CA 94550, USA; kcook@llnl.gov

⁸ Department of Astronomy, Pontificia Universidad Católica de Chile, Avenida Vicuña Mackenna 4860, 782-0436 Macul, Santiago, Chile; dante@astro.puc.cl

⁹ Department of Physics, Texas A&M University, 4242 TAMU, College Station, TX 77843, USA; suntzeff@physics.tamu.edu

Received 2010 April 19; accepted 2010 August 11; published 2010 October 29

ABSTRACT

We describe the first results from the Outer Limits Survey, an NOAO survey designed to detect, map, and characterize the extended structure of the Large and Small Magellanic Clouds (LMC and SMC). The survey consists of deep images of $55\ 0^{\circ}.6 \times 0^{\circ}.6$ fields distributed at distances up to 20° from the Clouds, with 10 fields at larger distances representing controls for contamination by Galactic foreground stars and background galaxies. The field locations probe the outer structure of both the LMC and SMC, as well as exploring areas defined by the Magellanic Stream, the Leading Arm, and the LMC orbit as recently measured from its proper motion. The images were taken with *C*, *M*, *R*, *I*, and *DDO51* filters on the CTIO Blanco 4 m telescope and Mosaic2 camera, with supporting calibration observations taken at the CTIO 0.9 m telescope. The *CRI* images reach depths below the oldest main-sequence (MS) turnoffs at the distance of the Clouds, thus yielding numerous probes of structure combined with good ability to measure stellar ages and metallicities. The *M* and *DDO51* images allow for discrimination of LMC and SMC giant stars from foreground dwarfs, allowing us to use giants as additional probes of Cloud structure and populations. From photometry of eight fields located at radii of 7° – 19° north of the LMC bar, we find MS stars associated with the LMC out to 16° from the LMC center, while the much rarer giants can only be convincingly detected out to 11° . In one field, designated as a control, we see the unmistakable signature of the Milky Way (MW) globular cluster NGC 1851, which lies several tidal radii away from the field center. The color–magnitude diagrams show that while at 7° radius LMC populations as young as 500 Myr are present, at radii $\gtrsim 11^{\circ}$ only the LMC’s underlying old metal-poor ($[M/H] \sim -1$) population remains, demonstrating the existence of a mean population gradient at these radii. Nevertheless, even at extreme large distances, the dominant age is significantly younger than that of the Galactic globular clusters. The MS star counts follow an exponential decline with distance with a scale length of 1.15 kpc, essentially the same scale length as gleaned for the inner LMC disk from prior studies. While we cannot rule out the existence of undetected tidal features elsewhere in the LMC periphery, the detection of an ordered structure to 12 disk scale lengths is unprecedented and adds to the puzzle of the LMC’s interaction history with the SMC and the MW. Our results do not rule out the possible existence of an LMC stellar halo, which we show may only begin to dominate over the disk at still larger radii than where we have detected LMC populations.

Key words: galaxies: evolution – galaxies: halos – galaxies: structure – Magellanic Clouds – techniques: photometric

1. INTRODUCTION, MOTIVATION, AND HISTORY

In our Galaxy, the most metal poor and (plausibly) the oldest stars are distributed in a halo that extends beyond 25 kpc.

¹⁰ NOAO is operated by the Association of Universities for Research in Astronomy, Inc. (AURA) under cooperative agreement with the National Science Foundation.

¹¹ Visiting astronomer, Cerro Tololo Inter-American Observatory, National Optical Astronomy Observatory, operated by AURA, Inc. under contract to the National Science Foundation.

¹² Current address: Astronomical Consultants, and Equipment Inc., P.O. Box 91946, Tucson, AZ 85752-1946, USA.

¹³ Physics Department, Harvard University, 17 Oxford Street, Cambridge, MA 02138, USA.

¹⁴ Space Telescope Science Institute, 3700 San Martin Drive, Baltimore, MD 21218, USA.

¹⁵ Also at Vatican Observatory, V00120 Vatican City State, Italy.

Their spatial distribution, chemical composition, and kinematics provide clues about the Milky Way’s (MW’s) early history, as well as its continued interaction with neighboring galaxies. In structure evolution models, the Clouds ought to have similar but scaled down accretion histories as L^* galaxies, and ought to have dark (and presumably also stellar) halos. Interaction with the MW should begin to strip away these halos, with a rate depending on the ratio of masses of the galaxies, on the perigalacticon distances, and the time spent in the “tidal region.” Thus, questions like the following must tell us about the formation and interaction histories of the Clouds. How old are the oldest stars in the extremities of the Clouds? How far do such stellar distributions extend? What tidal structure is revealed? Is there a continuity in the stellar distribution between the Large Magellanic Cloud (LMC) and Small Magellanic Cloud (SMC)? Do they share a common halo with the Galaxy? What

do the kinematics of stars in outlying regions tell us about the dark matter distribution? Do they shed any light on the orbital histories of the Clouds?

Two Micron All Sky Survey and DENIS are examples of panoramic surveys which have yielded fundamental information about the LMC disk: van der Marel (2001), using star counts of red giant branch (RGB) and asymptotic giant branch (AGB) stars, derived the tilt of the LMC disk against the sky, its intrinsic elongation, and its scale length. These probe stars fall off in density with distance from the LMC center, and eventually become too sparse to be usable: thus the structure beyond 10° , which is well within the LMC's estimated tidal radius (Weinberg 2000), remains unknown. As a result, much of the extant evidence for an LMC halo is indirect. Feast (1968) found that velocity dispersions of planetary nebulae exceeded that of H II regions, suggesting a spheroidal component. Schommer et al. (1992) demonstrated the same from the kinematics of old clusters, but also argued that the dispersion ($\sim 30 \text{ km s}^{-1}$) is not large enough for an isothermal halo, and that the old cluster kinematics are consistent with disk rotation. The inner RR Lyrae stars define a disk with characteristics similar to those obtained from AGB stars and Cepheids (Subramaniam & Subramaniam 2009). Minniti et al. (2003) obtained velocity dispersions of RR Lyrae stars distributed over the bar of $53 \pm 10 \text{ km s}^{-1}$, which has been taken as evidence that a halo exists. However, given that these reflect conditions over the projected center of the galaxy, it is not clear whether we are seeing a full-fledged halo, or just the central bulge.

Weinberg (2000) showed, assuming the older LMC space velocity, that LMC disk orbits are affected by the tides caused by the MW. These tides thickened the disk and created a set of "halo" objects rotating with the plane, thus explaining the results of Schommer et al. (1992) and Freeman et al. (1983).

Direct detection of spatially extended structure in the LMC/SMC is difficult, because of the considerable extent on the sky that such an entity would occupy, and because the LMC bar and disk are relatively face on. Irwin (1991) counted stars over an extended area from UKSTU plates: his isopleths show that there is a steep decline in stars near 8° from the LMC and near 4° from the SMC (suggesting a termination of their respective disks) but that tenuous structure persists over an apparent size of $23^\circ \times 17^\circ$ with "halos" of LMC and SMC overlapping. Kinman (1991) counted extra-tidal RR Lyraes around NGC 1841 and Reticulum (11.5° and 15° from the LMC bar) and found them consistent with a King model with 22 RR Lyrae stars per square degree over the LMC bar. On the other hand, while these RR Lyrae have velocities and distances consistent with LMC membership, Suntzeff et al. (1992) and Alves (2004) have argued that the data are also consistent with an extended disk model. Alves (2004) further noted that the best-fit *exponential* fit to the radial run of RR Lyrae stars has a scale length that matches that "of the LMC's blue light," i.e., of its bona fide disk.

Stryker (1984) found intermediate age blue stars in the color-magnitude diagram (CMD) as far out as 9.5° from the LMC center, near the globular cluster NGC 2257. A deep CMD 8° north of the LMC center by Gallart et al. (2004) also shows bright blue main-sequence (MS) stars (in addition to stars with fainter turnoff brightness showing ages from 8 to 13 Gyr), strongly suggesting the continued presence of young stars ($\sim 2\text{--}3$ Gyr), and thus of the disk. Dolphin et al. (2001) show that a field in the outskirts of the SMC also has a wide range of ages, from 2 Gyr old to at least 9–12 Gyr old. These results taken together show that we have not even begun to determine

how far any Cloud related structure extends and how its stellar content changes; and whether such structure is flat and disklike, or whether dominated by a spheroidal halo.

The survey presented here, which goes out to fields as far as 20° from the LMC and to $\sim 12^\circ$ from the SMC, is extreme compared to the spatial positions of other deep CMDs such as Gallart et al. (2004). However, there are some other shallower studies to note: Nidever et al. (2007) and Majewski et al. (1999, 2009) claim detection of LMC red giant stars out to at least 23° from the LMC center, with LMC-like velocities. Munoz et al. (2006) see stars in the field of the Carina dwarf spheroidal that they interpret to be from the LMC, at an angular distance of 22° from the LMC.

van der Marel et al. (2002) analyze the carbon star velocities in the LMC samples of Kunkel et al. (1997) and unpublished work by Hardy, Schommer, & Suntzeff, taking care to account for the full effects of the LMC's space motion on the radial velocity distribution of the carbon stars. They find that the LMC disk has a rotation curve amplitude of $50 \pm 16 \text{ km s}^{-1}$, that more than half of the $\sim 9 \times 10^9 M_\odot$ enclosed within $\sim 9 \text{ kpc}$ is due to a dark halo, that the disk is thick and is tumbling at a rate $di/dt = -103^\circ \text{ Gyr}^{-1}$. They also measure a dynamical center and position angle of the kinematic line of nodes consistent with those expected from their geometric studies of the shape of the LMC disk (van der Marel & Cioni 2001; van der Marel 2001), lending support to their analysis. Olsen & Massey (2007) compare the LMC's carbon star kinematics with those of its red supergiants (Massey & Olsen 2003) and H I (Kim et al. 2003), while employing the updated LMC proper motion measurement of Kallivayalil et al. (2006). They find a larger rotation curve amplitude of $\sim 60 \text{ km s}^{-1}$ for the carbon stars, with larger values still for the H I and red supergiants. They also conclude that $\sim 10\%$ of the carbon stars are being stripped along with H I in tidal streamers. In contrast, the Magellanic streams, which are the most extreme examples of disturbances and flows, have shown no evidence to date of corresponding stars. It is thus important to see if evidence for stripping can be found farther out from the LMC center, where, if anything, tidal effects are expected to be more pronounced.

It is worth noting here that while the term "halo" has been used to label a tenuous extended spheroidal component (as gleaned from diffuse surface brightness) around galaxies other than our own, it is only in our own Galaxy, that the dynamical behavior is also known. There continues to be confusion about whether so-called halos around galaxies are just a continuation of their bulges (in which case the late-type spirals should have progressively weaker halos), or whether they are determined by some other process. Understanding the dynamical properties of halos can provide clues, but spectroscopy of faint stars in all but the nearest galaxies is beyond current reach. This was another strong motivation in the design of this survey: finding objects that can be used as dynamical tracers in the outermost regions of the Clouds.

Given this current state of knowledge, we wish to address the following questions.

1. How far do the disk structures of the LMC and SMC extend?
2. Are there stars in an extended spheroidal distribution (halo), as in the MW? Λ CDM cosmology predicts a spheroidal dark matter halo for galaxies like the LMC. Is there an accompanying stellar halo? What, if any, relation binds a stellar halo to the dark matter halos posited by the Λ CDM models? The LMC/SMC/MW system appear to be in the early stages of a merger, or a near merger. A detailed study

of the components of the individual galaxies will help us better interpret the imprints of past mergers in the current universe.

3. How do ages and metallicities change with position within each Cloud? What is the distribution of the *oldest* stars along the line between the LMC and SMC? What does this distribution reveal about the history of interaction of the two galaxies? Ages and metallicities from this survey will tag intermixing of LMC–SMC–Galaxy–halo populations in the boundary regions.
4. Are there stars associated with the Magellanic Stream? Our survey re-addresses this issue with much higher sensitivity.
5. What do the dark matter halos of the Clouds look like? The survey is designed to identify *individual* red giants associated with the Clouds from foreground dwarfs using gravity sensitive photometry comparing *DDO51* and *M* (see Geisler 1984; Morrison et al. 2001, and references therein), a method that works even better when the giants are more metal poor than the foreground dwarfs in the MW. The giants can serve later as kinematic probes for tracing the potential and how it changes going between the Clouds and the Galaxy. This provides a probe for the dark matter halo(s), whose presence is predicted by the Λ CDM cosmology.

2. SURVEY GOALS AND OBSERVATIONAL DESIGN

We have carried out deep imaging in selected fields within an extended region around the LMC/SMC complex, up to radial distances of 18 kpc in projection from the LMC, and ~ 12 kpc from the SMC in order to examine the disk and/or halo structure of the Clouds at larger radii than have been reliably examined before. We have also included pointings in various spots within and outside both the “leading” and “trailing” sections of the Magellanic Stream, to look for their elusive (Majewski et al. 2003) stellar content, which should be present if these streams have tidal origin.

MS stars are the most unambiguous tracers of any stellar population, and photometric information in appropriate passbands can reveal metallicities and ages. The LMC/SMC are at just the right distance to see substantial portions of the MS with ground-based wide field imaging (seeing limited to ~ 1 arcsec) before contamination from unresolved background galaxies becomes important. Also, unevolved stars in this unambiguous portion of the MS out-number the corresponding more luminous evolved giants by a factor of ~ 100 . For these reasons, we chose to set up a five passband system that concentrates on the MS, while still studying the giants.

The data from our survey, whose observational design is laid out in the remainder of this section, are crafted to enable us to learn about the early history of the LMC and SMC, and about their interactions with each other and with the MW, by focusing on the questions listed at the end of Section 1.

2.1. Passband Selection

The filter choice for this survey is a hybrid of Landolt *R*, *I*, and Washington *C*, *M* (Canterna 1976), with *DDO51* (Geisler 1984). Their respective functions will be described in more detail in Section 4, where we will show that CMDs from this set allows us to (1) discriminate metallicities to within a factor of two, (2) constrain ages to 20%, even for ancient populations, (3) map spatial densities, metallicities, and ages over a much wider outer expanse of the LMC/SMC complex than ever before,

with much greater sensitivity than previous studies, and (4) pick out red giants associated at the distance of the Clouds by discriminating against the plethora of foreground Galactic red dwarfs, so that future spectroscopic observations can furnish kinematic and detailed chemical composition data.

For most fields foreground reddening is modest ($E(B - V) \leq 0.1$), and can be obtained from dust maps (Schlegel et al. 1998) or even more direct means. For the majority of our fields, which are quite far out from either the LMC or the SMC, extinction from within these galaxies is expected to be insignificant. In any case, as we shall see later, the actual data and resulting CMDs in multiple bands effectively delimit the possible range of total extinction in a given field, if self-consistent comparison with isochrones is demanded. In particular, note that since to zeroth order both *C* and *M* passbands track metallicity, such sanity checks from *CMRI* photometry are effective, even though metallicity is an unknown.

2.2. Survey Requirements and Exposure Details

Exposures times were calculated according to the following stipulations.

1. *C*, *R*, and *I* images must reach at least 1.5 mag past the turnoff brightness of stars for an old globular cluster placed at the distance of the SMC (the farther of the two Clouds), with a signal-to-noise ratio (S/N) ≈ 20 or better. This corresponds to $R \approx 24.0$, $I \approx 23.5$, and $C \approx 24.5$. This is required to enable identification of a section of the MS that is populated by stars of all ages.
2. The photometric S/N on the giant branch of a globular cluster at the distance of SMC must be ≈ 50 or better. This drives considerable attention to the containment of systematic errors in the photometry, and is necessary if we are to be able to compare systematically between different fields, differentiate reddening effects and discriminate metallicities.
3. Photometry in *M* and *DDO51* should have S/N ≈ 50 on the SMC giant branch, with no requirements for fainter magnitudes (i.e., not planned for use on the MS stars at Cloud distances).
4. Short exposures that do not saturate AGB stars at the LMC distance must also be taken in all five passbands.

To meet the above stipulations, a large range of brightness must be covered. To do so, the exposures in the various passbands were made up as follows.

1. *R*: $3 \times 580 \text{ s} + 1 \times 50 \text{ s} + 1 \times 10 \text{ s} = 1800 \text{ s total}$.
2. *I*: $4 \times 585 \text{ s} + 1 \times 50 \text{ s} + 1 \times 10 \text{ s} = 2400 \text{ s total}$.
3. *C*: $3 \times 1080 \text{ s} + 1 \times 300 \text{ s} + 1 \times 60 \text{ s} = 3600 \text{ s total}$.
4. *M*: $2 \times 120 \text{ s} + 2 \times 30 \text{ s} = 300 \text{ s total}$.
5. *DDO51*: $2 \times 750 \text{ s} + 2 \times 150 \text{ s} = 1800 \text{ s total}$.

Thus, each field takes 2.75 hr of exposure time, and with pointing and read-out overheads, a total time of about 4 hr. The data were acquired in several observing runs using MOSAIC2 on the Blanco 4 m telescope at CTIO, spanning more than a two year period from 2006 August, through 2008 December, in addition to some data from a pilot program (with the same instrument and telescope) from 2005 October. Approximately 20% of the total time was lost to weather or inadequate seeing conditions. Exposures were *not* dithered. On occasion, when the same field was observed on different observing runs, there were small unplanned offsets in the pointing.

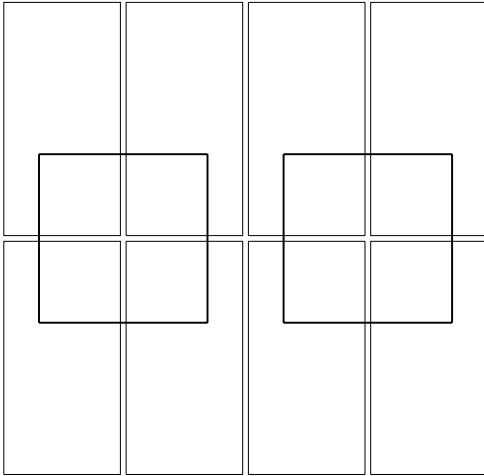


Figure 1. Schematic diagram drawn to scale on the sky, showing the relative placement of the eight $2K \times 4K$ CCDs of MOSAIC2 shown as faint rectangles and of the two pointings on the CFCCD shown as the bold squares. With two pointings of CFCCD, there are common stars between CFCCD and each of the eight CCDs of MOSAIC2.

2.3. Photometric Calibration

Realizing that there are times when useful imaging can be obtained even though pristine photometric conditions do not prevail, and also because observing standard stars with MOSAIC2 is relatively inefficient, we chose to acquire auxiliary data to calibrate our observations. The 0.9 m with the CFCCD imager on CTIO was used to observe standard fields, as well as parts of each MOSAIC2 target area. These observations were not on the same nights as the MOSAIC2 data. Only 0.9 m data obtained in photometric conditions (as gleaned a posteriori from the photometry residuals of standard stars throughout the night) are used. Of the 22 nights allocated for the 0.9 m telescope in the period between 2006 August and 2009 December 14 were deemed photometric, with standard star rms residuals in all bands of at most 0.025 mag. These observations establish local sequences on each MOSAIC2 field and eliminate the need to observe each field with MOSAIC2 in perfect photometric conditions. On each night of observing with the CFCCD, target object fields were interspersed with standard star fields from Landolt (1983, 1992) that also contain stars that have been calibrated for Washington *C* and *M* (as detailed in Section 3.5).

The CFCCD on the 0.9 m covers a field area of 13 arcmin on a side. Figure 1 shows the two positional placements of the CFCCD with respect to the eight chip format and area coverage of the MOSAIC2 field of view (FOV). Thus for each field observed with MOSAIC2, the plan calls for two placements of the CFCCD, which allows secondary photometric sequences to be established on all eight MOSAIC2 CCDs. In practice, there are photometric data in both pointings for only half of the fields of Table 1. However, all of the fields have at least one CFCCD placement to establish the photometry. Details of the process and measures of accuracy are deferred to Section 3.2.

2.4. Field Selection

A complete survey around the LMC/SMC complex, covering from 8° to 20° distance from each of the galaxies, the “bridge” region in between, and in and around the Magellanic Stream requires a coverage of over 2000 deg^2 . Currently the most

Table 1
Designations and Central Coordinates of Survey Fields

Field Name	Gal. Long. ℓ°	Gal. Lat. b°	R.A. (J2000) (hh:mm:ss)	Decl. (J2000) ($^\circ$: $'$: $''$)
C1	330	-15	17:34:00	-62:36:00
C2	330	-30	19:45:40	-65:36:00
C3	330	-45	22:00:40	-61:42:00
C4	330	-60	23:20:26	-52:42:00
C5	0	-75	23:50:40	-34:00:00
F506	310	-45	23:55:00	-71:20:00
F504	313	-45	23:25:00	-70:24:00
F503	316	-45	23:03:52	-69:18:00
F502	319	-45	22:52:43	-68:05:45
F501	322	-45	22:35:28	-67:06:42
F307	301	-55	1:05:58	-62:31:59
F305	301	-57	0:57:02	-60:10:02
F304	301	-66	0:56:17	-51:00:42
F306	300	-70	0:59:52	-47:20:19
F308	299	-57	1:13:34	-60:33:50
F309	295	-57	1:21:27	-59:34:45
F301	308	-58	0:30:51	-58:37:33
F508	310	-50	0:04:31	-66:22:33
F507	307	-45	0:04:02	-70:59:48
F521	309	-47	0:05:00	-69:35:00
F4C1	290	-20	8:48:49	-76:14:31
F4C4	294	-8	11:10:52	-68:56:34
F4C6	285	-15	8:58:34	-69:22:14
F411	300	-20	11:35:08	-82:36:43
F412	303	-15	12:47:08	-77:59:30
F414	308	-8	13:45:33	-70:31:32
F415	310	-5	14:06:40	-66:45:55
F404	295	-25	7:49:36	-82:46:02
F405	295	-20	9:43:47	-80:01:53
F111	263	-35	5:20:25	-55:20:15
F113	265	-31	5:48:49	-57:02:20
F7N	272	-34	5:23:34	-62:45:00
F9N	269	-34	5:23:34	-60:45:00
F11N	267	-34	5:23:34	-58:45:00
F12p5N	265	-34	5:23:34	-57:15:00
F14N	263	-34	5:23:34	-55:20:00
C20	245	-25	6:04:38	-38:25:35
C18	245	-35	5:15:20	-40:43:05
C14*	245	-55	3:28:35	-40:23:56
C12	245	-65	2:40:32	-38:03:50
C102	225	-75	1:58:00	-29:30:00
F605	283	-50	2:45:57	-62:39:45
F603	290	-48	2:21:24	-66:54:24
F601	297	-43	1:53:46	-73:36:10
F531	312	-45	23:32:08	-70:41:27
F532	310	-43	23:41:16	-73:08:22
F533*	310	-47	23:55:20	-69:28:35
F534	304	-46	0:43:21	-70:54:00
F121*	258	-34	5:21:50	-50:28:16
F122	260	-34	5:21:59	-52:05:33
F123	258	-34	5:24:43	-54:02:27
F141	269	-26	6:26:15	-59:39:12
F142	268	-25	6:36:55	-58:47:40
F143	266	-23	6:40:55	-56:50:34
F144*	265	-22	6:50:45	-55:14:38

Note. Fields marked with “*” have missing observations, but the partial available data are useful enough.

efficient instrument complement available that can be pointed at the desired region of sky is the combination of the CTIO 4 m Blanco telescope and the MOSAIC2 imager. A complete survey is unfeasible, since each pointing with MOSAIC2 (eight CCDs,

each with $2\text{K} \times 4\text{K}$ pixels) covers only 36×36 arcmin² or 0.36 deg² of sky. A “reasonable” survey program of 30 nights covers 50–60 pointings, at least 10% of which need to be on control fields. This allows only about a 1% fill-factor of the region of interest, so the fields must be chosen purposefully. With the LMC and SMC interacting with each other, and both interacting also with the Galaxy, we should not expect much spatial symmetry. We must, at a minimum, observe along several directions, each of which we expect to either be dominated by, or least affected by key aspects of the LMC/SMC/Galaxy interactions, so that we may attempt to disentangle them.

Accordingly we focused attention on five regions.

1. Looking away from the LMC in a direction least complicated by the SMC. This is along north from the LMC from about 7° to 20° from the LMC center, which is past the nominal tidal radius of the LMC. These fields are labeled F7N, F9N, F11N, F12p5N, F14N, F121, F122, and F123, with two flanking fields F111 and F113. Additional fields (designated as F141, F142, F143, and F144) at distances from 11° to 17° running NW from the LMC were also chosen to sample more outlying fields with the original goal of searching for tidally stripped stars predicted by Weinberg (2000).
2. Almost due north from the SMC along the Magellanic stream. These field designations begin with “F3.”
3. Toward the Galactic plane from the LMC along the “leading arm” of the Magellanic Stream (Putman et al. 1998). These field labels begin with “F4.”
4. Away from the LMC/SMC complex, westward from the SMC, orthogonal to the Stream, which is also an area opposite from the LMC and so least affected by it. The names begin with “F5.”
5. Several control fields 30° – 40° away from the Clouds, spanning a range of Galactic latitudes that bracket the levels of foreground contamination in our target fields. This is necessary to make good models to account for contamination. These field names begin with “C.”
6. In a direction looking back along the LMC’s trajectory, based on the proper motion studies by Kallivayalil et al. (2006) and Piatek et al. (2008). Designations begin with “F6.”
7. We had originally planned fields along the line between the SMC and LMC (the bridge): to test how the two galaxies interact near their extremities. These were not executed in the end, but very similar data were obtained in an independent program by one of us (Harris 2007).

The list of target fields actually observed is given in Table 1, indicating field centers in both equatorial and Galactic coordinates. Of these, 45 have designations beginning with the letter “F” and were chosen because their locations address one or more of the survey goals, as described above. In addition there are 10 fields beginning with “C,” which were designed as control fields for sampling background and Galactic foreground contamination. Our total region of interest spans a large range in Galactic latitude and longitude, so these control fields are necessary to trace changes in the Galactic foreground. The control fields were chosen to be far enough away from either Cloud, so that the LMC/SMC complex cannot be expected to contribute to the star counts at their locations. Figure 2 shows the locations of these fields in the spatial context of the LMC, SMC, Galactic Plane, and H I in the Magellanic Stream, using results from the GASS survey (McClure-Griffiths et al. 2009). Three of the

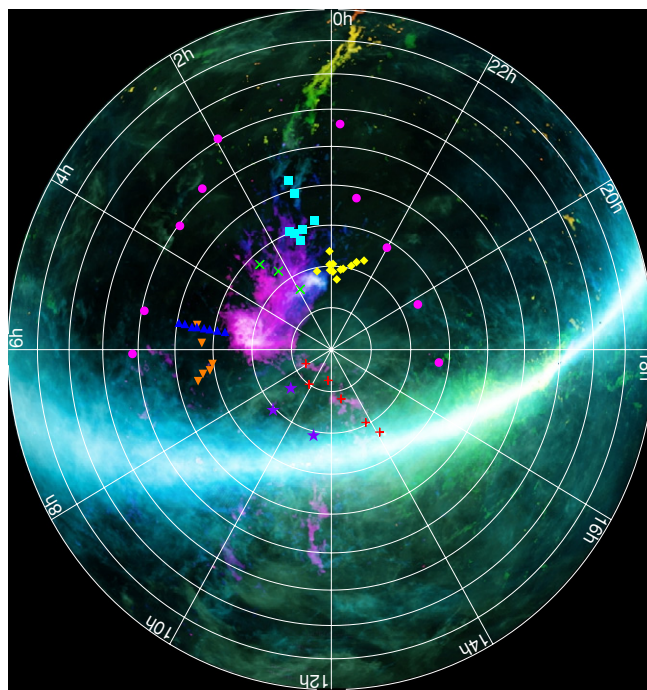


Figure 2. Extended region of the sky surrounding the Magellanic Clouds, as seen in neutral hydrogen emission. The Galactic plane, the location of the LMC and SMC, and both “leading” and “trailing” arms of the Magellanic Stream are clearly visible. The positions of the fields studied in this survey are shown by the overplotted symbols. The main control fields are marked with purple filled circles, and the ancillary control fields whose designations begin with “F4C” are shown as purple asterisks. The fields marked in blue triangles are the ones going away due north from the LMC, roughly parallel to the Galactic plane. The orange triangles show other fields that trace the extended LMC structure, with designations beginning with “F1.” Fields tracing the trailing arm of the Magellanic stream are shown as light blue squares: their designations begin with “F3.” Red crosses mark fields along the leading arm of the stream, designations begin with “F4.” The yellow squares show fields with names beginning in “F5,” designed to trace the extended structure of the SMC. The blue crosses cut across the line of motion of the LMC and designations begin with “F6.” Image credit: S. Janowiecki and the Galactic All Sky Survey (McClure-Griffiths et al. 2009).

fields have mixed designations (F4C1, F4C4, and F4C6): they are low Galactic latitude, and are of interest in themselves, but they were also intended to serve as comparison fields against those that lie on the “leading arm” of the Magellanic Stream.

3. DATA PROCESSING

3.1. Processing of MOSAIC2 Images

The raw images from the MOSAIC2 were de-biased and flat-fielded using dome flats (sky flats to correct for illumination did not improve overall flatness) and the standard IRAF¹⁶ tools in the MSCRED package. The world coordinate systems (WCS) were derived and applied to each image, using the routines MSCR-PEAK or MSCSSETWCS plus MSCCMATCH, and matching against the USNO-B1.0 astrometric catalog stars (Monet et al. 2003). With coordinates well established (typical rms errors of 0.2 arcsec), the multi-extension FITS files containing the eight image sections from the eight separate CCDs were then processed by the MSCIMAGE routine in MSCRED to create a single image that is a gnomonic projection. For any given target field, the position on the sky of one specific CCD corner

¹⁶ IRAF is distributed by the National Optical Astronomy Observatory, which is operated by the Association of Universities for Research in Astronomy (AURA) under cooperative agreement with the National Science Foundation.

at the center of the mosaic for one of the long R exposures was defined as the tangent point for all images in all bands of that field. By this design, the projected images have pixels of equal area. To zeroth order, they have the same pixel size as the original image, but higher order terms correct the geometrical distortions of the MOSAIC2 imager, and re-map the spherical co-ordinates of the sky onto a plane. Individual images of a given field can then be cross-registered in position by simple translation in the projected image plane, and co-averaged with the COMBINE routine in IRAF, using position offsets driven by the fitted WCS.

The geometrical distortions in the MOSAIC camera means that pixels in different places in the FOV see slightly different solid angles on the sky. The flat-field corrections, which have the net effect of mapping pixel value to surface brightness, induces a systematic error to aperture fluxes from point sources. Re-mapping the image to equal solid angle pixels by *resampling*, as opposed to conserving the pixel value sums in the flat-field corrected images, has the salubrious effect of restoring the image so that aperture fluxes are on an equal basis across the field. It is important that the stellar point-spread functions (PSFs) be well sampled for this to work, a criterion that is always met for our data.

Nonetheless, any re-binning of data generates correlation in the noise across neighboring pixels, while ignoring any pre-existing noise correlations that already exist in the input image. Every PSF fitting code known to us implicitly assumes that there is zero correlation of noise among neighboring pixels, so processes that increase correlation should be kept minimal. Well-sampled PSFs help to suppress errors from this source. A second effect is that that a spatial pattern in the noise is introduced due to “beating” of the old and new pixels, generating a Moire pattern in the noise. To first order, both these effects result in increased noise in the photometry. For an ensemble of objects taken over a significantly large patch of the image, the net scatter is increased, but there should not be systematic effects introduced for such an ensemble (although for a single given object there may be subtle systematic effects involved, especially if images are under-sampled, which the MOSAIC2 images are not). We have been diligent in watching for these effects, as discussed later in Section 3.2.1.

For each field, there are three final images in each of C , R , and I to cover the wide range of brightness.

1. A deep image obtained by an S/N-weighted co-average of all images in that band. Many stars in this image are saturated.
2. A medium image obtained similarly by co-averaging the two shorter exposures (for R and I the 50 s and the 10 s exposures, and for C , the 300 s and 60 s exposures). Only the brightest stars are saturated in this image.
3. A short image, which is just the shortest image obtained (i.e., 10 s exposure for R and I , and 60 s exposure in C). All stars fainter than 12th magnitude should be unsaturated in these images.

For M and $DDO51$ images, only two final images are made in each band:

1. A deep image which is the S/N-weighted co-average of all images in that band;
2. A short image which is the co-average of the two short images (i.e., 30 s exposures in M and the 150 s exposures in $DDO51$).

The final images are masked as needed, so that any regions not exposed (such as gaps between CCD chips) in all the component images are fully suppressed for subsequent analysis. All saturated pixels are assigned a large negative number value that the subsequent photometry programs interpret as missing data. The FITS headers of the final combined images were edited manually to carry the correct values of GAIN (in electrons per ADU) and read noise (in electrons), correctly reflecting their propagation through the COMBINE processing. Thus, in the end, for each field, there are 13 final images. Each image is geometrically flat and fitted with an accurate WCS. They each carry the correct values of gain and read noise, as well as the correct effective exposure time to which the co-averaging is scaled. These images and photometry are being placed in the NOAO archive, as papers are published.

3.2. Instrumental Photometry from MOSAIC2 Images

Each of the 13 final images (as described above) of any given field is then run through a process constructed around a variant (by one of us: Saha) of the DoPHOT photometry program (Schechter et al. 1993).

First, an IDL based routine written by us (Brondel & Saha) finds the brighter objects, does a rudimentary rejection of galaxies and cosmic-ray-like features by examining image roundness and sharpness. It uses this preliminary set of what must be stellar objects, to derive an analytic PSF in the form expected by DoPHOT.

Using the above derived initial PSF estimate, DoPHOT is run on the image. In addition to the list of objects and PSF fitted photometry, this variant version also generates aperture magnitudes for a range of aperture sizes of the bright high S/N stars, which are measured in isolation, i.e., with all other objects subtracted. There are two sets of aperture sizes: set A for aperture sizes from 2 to 16 pixel radius in steps of 2 pixels and set B for aperture radii from 4 to 32 pixels in steps of 4 pixels. For set A, for each star to which the procedure is applied, the sky subtracted is that scalar value for which the dispersion in measured brightness for apertures sizes 10, 12, 14, and 16 pixels is minimized, and for set B the sky value subtracted is similarly that for which the dispersion in brightness for 20, 24, 28, and 32 pixels is minimized. In effect this procedure seeks that value of sky for which the growth curve is as flat as possible for the outlying apertures of each set. The rationale for these two sets of apertures is explained below.

The set B aperture magnitude at 20 pixel (~ 5.4 arcsec) radius, denoted by m_{20} is the aperture to which we wish to refer all measured magnitudes. For images with seeing ≤ 2.0 arcsec FWHM, it is deemed to contain all of the incident light from a star, except that which is scattered by the telescope and instrument optics. Even though the seeing may vary from one image to another, all of the seeing induced broadening is asserted to be within this aperture. Another way of saying this is that the fraction of light from a star which falls outside this aperture is from scattering, which does not change (in any given passband) from exposure to exposure. Thus, as long as the seeing is not larger than 2.0 arcsec FWHM, all stars in all exposures send the same fraction of their light outside this aperture. Thus, m_{20} can be used as an instrumental magnitude, in the sense that it measures the same fraction of light that reaches the telescope from a star for all stars in all exposures. We must map the PSF fitted magnitudes (denoted by m_{fit}). If the PSF is constant within any given exposure, then all that is needed is to calculate $\langle m_{20} - m_{\text{fit}} \rangle$ using the brighter stars, and apply this aperture

correction to the fitted magnitudes: this is common practice for instruments where the PSFs are in fact invariant over the (usually small) FOV. A test for the validity of a constant PSF is to look for position dependent trends in $m_{20} - m_{\text{fit}}$. For our MOSAIC2 data, this test shows significant trends, and a total scatter that in the worst situations can be as large as 0.2 mag! Efforts to characterize the systematics of this variation were thwarted by the fact that due to the large aperture sizes, only a few objects have high enough S/N measurements of m_{20} . The set A analog of m_{20} is m_{10} . One can make much higher S/N measurements of m_{10} because of the smaller aperture size. Many more stars can be measured with the required accuracy and subtraction of the fitted PSFs of neighboring objects has left fewer residues. The aperture correction systematics across the FOV for any given exposure can be far better traced using $m_{10} - m_{\text{fit}}$ as compared to $m_{20} - m_{\text{fit}}$. However, seeing changes from one exposure to another can induce small systematic differences, so it may be too small for use as an instrumental magnitude. So the procedure is broken into two parts: $m_{10} - m_{\text{fit}}$ of a relatively large number of stars is used to trace the aperture correction variations across the FOV of a given image and to apply suitable corrections (details below). In another step, the value of

$$\Gamma = \langle m_{20} - m_{10} \rangle \quad (1)$$

is evaluated from a few very high S/N stars, and applied as a further correction, which finally refers all magnitudes to the instrumental system of m_{20} .

Using $\Delta m = m_{10} - m_{\text{fit}}$ to trace the aperture correction systematics has proved to be very revealing.

1. The variations in Δm_{10} across the FOV are most acute when the seeing is best. This is when the PSF variations across the field are also the most prominent, so this confirms that the aperture correction variations are induced by PSF variations.
2. The variation of Δm_{10} is smooth across any part of the FOV covered by the same CCD chip, but there can be discrete jumps from one chip to the next. Fitting a single chip with a surface linear in x and y significantly reduces the scatter of Δm_{10} within the area spanned by that chip, but rarely eliminates it completely.

These results suggest that small misalignments between the chips could be the source of much of the Δm_{10} variation. Each chip is slightly non-orthogonal to the optical axis, which a linear term in x and y corrects, and each chip has its own positional offset from nominal along the optical axis, resulting in different constant additional terms. We also tried fitting a quadratic surface and found that in all instances the scatter in the residuals reduces to levels consistent with the measurements errors. Relatively large non-orthogonality in position can also result in quadratic terms and is a possible explanation. However, further investigation reveals that the quadratic terms are highly correlated across the chips. To understand this better, we examined the residuals after applying a linear surface correction to the individual chips, but studied them as a whole across the entire FOV. We found a pattern in these residuals that is well fitted by a single radially symmetric quadratic term. Further, in the most pronounced instances of Δm_{10} variation, it is this component that dominates.

The origin of this radially symmetric variation in aperture correction almost certainly lies in the interaction between the detector and focal surfaces. The true focal surface is a bowl, and the idealized detector surface is flat. The intersection of

these two surfaces is the locus of best focus, and clearly the PSF can be expected to vary as the space between the two surfaces changes with position on the FOV. This is illustrated schematically in Figure 3. The straight thick line at zero ordinate is the detector plane. The ideal focus is where the curved focal surface is set so that equal areas of the detector plane lie on opposite sides of the surface: this is represented by the full line that intersects the detector plane. Less optimal focus positions are shown by the various dashed lines, where the focal surface is positioned non-optimally with respect to the detector plane. This graphically illustrates how differences in focal placement drive quite different variations of the PSF with position on the FOV. Note that the aperture correction variations are unique for each image and must be evaluated independently for each image on which photometry is being done.

At the end of our experimentation, it was determined that the most robust constraints of the aperture correction variation as a function of the position on the FOV are obtained by fitting the following elements simultaneously.

1. A quadratic surface symmetrical about the image center (assumed optical axis intersection).
2. A linear surface (plane), including offsets determined independently for each section spanned by a different CCD chip in the FOV.

Denote the final surface fit to Δm_{10} by $\Sigma_{10}(x, y)$. If m_{fit}^i is the PSF fitted magnitude of the i th star on the image at hand, and if it is located at position (x, y) , then we can write

$$m_{\text{inst}}^i = m_{\text{fit}}^i + \Sigma_{10}(x, y) + \Gamma, \quad (2)$$

where m_{inst}^i is now the 10 pixel aperture equivalent magnitude propagated from the PSF fitted magnitude, but on the system of a 20 pixel (~ 5.4 arcsec) radius aperture.

Routines to fit the surfaces were custom written in IDL by us (Saha & Brondel), and use weighting schemes that follow the error estimates for each object as generated by DoPHOT.

Further calibration of the objects requires establishing reference to standard stars and is discussed after we describe the processing of the calibration images obtained with the 0.9 m telescope.

3.2.1. Implications of Image Re-sampling on the PSF Fit Photometry

The MOSAIC2 images are well sampled in all instances, even in the best seeing we encountered. In principle, a single resampling of the images using sinc interpolation should not produce noticeable systematic errors in the aperture referenced magnitudes derived as above. Nevertheless, in order to verify this empirically, we ran several test comparisons, where we compared the photometry performed on un-rebinned data on individual chips of single exposures (corrected for pixel area variations derived from WCS fitting) against that from the corresponding images as processed above. The comparisons are very satisfactory, with chi-square values (error estimates from DoPHOT) that are significantly smaller than unity (i.e., the differences are smaller than the Poisson S/N errors).

3.3. Processing of the 0.9 m CFCCD Images

The raw images obtained with the CFCCD on the CTIO 0.9 m telescope were corrected for bias and flat-fielded (using a combination of dome and twilight flats taken on the same night), using the QUADRED package in IRAF. During each observing run, daytime observation of the dome flat-field source was used

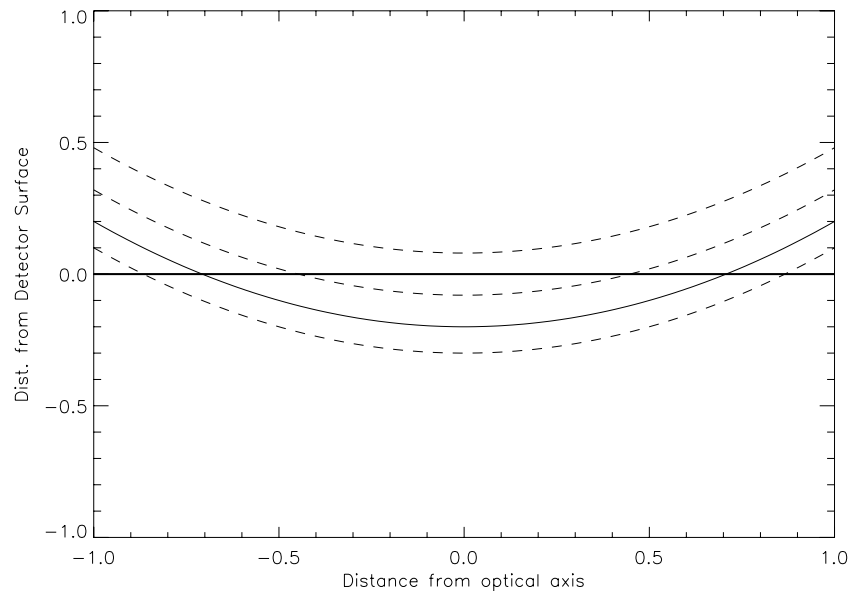


Figure 3. Illustration of how variations in the PSF across the FOV can arise because the focal surface is not an exact match to the detector surface. The detector surface, here idealized as a perfect plane, is viewed edge-on: the horizontal line at ordinate zero is the detector plane. The optical axis is vertical and intersects the detector surface at the center. The surface of best focus, imperfectly matched to the detector plane, is shown as a curve. The solid curve corresponds to an optimal compromise focus position, with equal areas of the detector plane on either side of the focal surface. It is clear that the farther away a given point on the detector is from the focal surface, the more the PSF is degraded. Sub-optimal focusing, where the position of the focal surface with respect to the detector plane is shown by the dashed curves, makes the situation worse. If the detector surface is not a perfect plane orthogonal to the optical axis, then that too will contribute to the run of PSF variation across the FOV. In the case of MOSAIC2, in reality the detector surface is in eight planar sections, each with its own imperfection in alignment with respect to the ideal detector plane.

to create a shutter timing/shading correction: this is a correction *image* that is used to correct both the short exposure flat fields (especially of the twilight sky) and all target exposures so that the intensity at every pixel of the image is scaled from how long that pixel was really exposed to the nominal exposure time for that image.

The data were taken so there are always a pair of images in each of the four bands (R , I , C , M). However, the images were not combined: photometry was performed independently on each exposure, and then merged, using error estimate weighted averaging, and propagating the resulting uncertainties. For this reason, there was no compelling reason to resample the images. Any variations of pixel size as projected on the sky were corrected using a pixel-area correction derived from the WCS solutions and the images scaled accordingly.

3.4. Instrumental Photometry from CFCCD Images

The photometry process was like the one described above for the MOSAIC2 images, except for a few differences in parameters resulting from differences in the pixel scale, and the fact that there is only one CCD chip, and thus only one correction for the tilt between the detector and focal surfaces. Accordingly, the set A aperture sizes in pixels for the CFCCD data were identical to those for the MOSAIC2 data. However, here the equivalent m_{10} corresponds to ~ 4 arcsec. The set B apertures for CFCCD were 3, 6, 9, 12, 15, 18, 21, and 24 pixels in radius. In lieu of m_{20} used for the larger aperture magnitude for MOSAIC2 data, for CFCCD data we use m_{15} , which corresponds to ~ 6.0 arcsec, which on the sky is only 10% larger than used for MOSAIC2. In the correction from m_{fit} to m_{10} , Δm_{10} was fit to a quadratic surface symmetrical about the center of the FOV. Again, the complications that come with having multiple CCD chips do not appear here.

The final instrumental magnitude m_{inst} for the CFCCD is then the magnitude propagated from the PSF fitted magnitude,

but on the system of a 15 pixel (~ 6.0 arcsec) radius aperture. This instrumental magnitude is uncorrected for extinction from the terrestrial atmosphere, as is the case for the MOSAIC2 instrumental mags.

3.5. Calibrated Photometry from the CFCCD Data

On each night of observing with the CFCCD, target object fields were interspersed with standard star fields from Landolt (1983, 1992). These references furnish R and I values for several stars per field. Geisler (1996) provides C and M standards for select stars in SA92, SA98, SA101, SA107 and SA114, NGC 3680 and around PG0231+051. In an unpublished work, Saha has used observations from the WIYN telescope to establish C and M magnitudes of select stars in Landolt fields in SA92, SA98, SA110, Ru149, and M 15. Cross-comparison with photometry in Geisler (1996), and with additional unpublished photometry of the globular cluster M15 kindly provided to us by D. Geisler (2005, private communication) were used to achieve this calibration. These C and M standards in the Landolt fields are established to be internally consistent to $\sim 1\%$: for instance, the Saha set calibrated using only M15 inter-comparison predicts magnitudes of stars in SA114 that agree with the values of Geisler (1996) to better than 0.015 mag in the mean over the entire color range $0 < C - R < 5$. The observations of these chosen Landolt fields thus provide standard stars for both Landolt R and I , as well as for Washington system C and M bands.

For any given target, the instrumental magnitudes in the four bands for each target are collated. The object list from the R image is treated as the master. Objects from the other three filters are matched to that, on the basis of the position on the sky, with typically a 1 arcsec match tolerance. Thus, the collated list always has a measurement in R , but for faint objects, there may be drop-outs in one or more of the other bands.

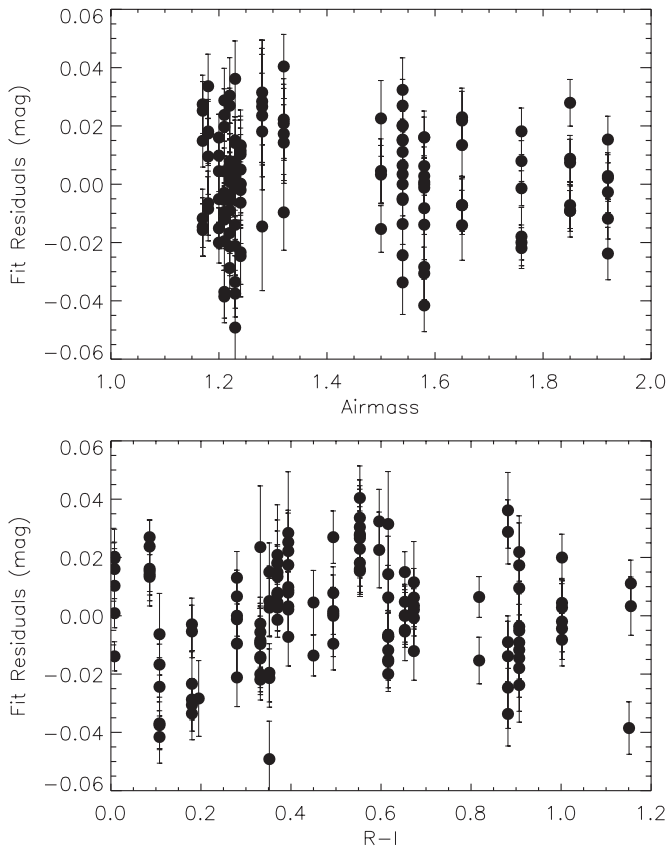


Figure 4. Fit residuals in the R band for the night of 2007 October 12, from CFCCD observations of standard stars. The upper panel shows the residuals against observation airmass, and the lower panel shows the same against the $R - I$ value of the respective standard star. There were 23 different standard stars, each observed several times. The error estimates for each measurement are shown: the solution used the inverse square of the error bars as weights. See Table 2 for the solutions for this night.

Consider the R band as an example. Denote the instrumental magnitudes by R' . First, R' for the standard stars are compared against their true values R . Allowing for variations due to extinction and color dependence, we solve for

$$R' = R + \alpha + \beta X + \gamma \text{COLOR}, \quad (3)$$

where R is the true magnitude, X is the airmass at which the observation was made, and COLOR is a suitable quantity, e.g., $R - I$, and α , β , and γ are coefficients that are solved for, using many measurements of several standard stars described above (>100 measures in each of R and I , and >60 measurements in each of C and M per night) spanning a wide range of colors, and airmass range from $1.2 < X < 2.1$. All fitting uses individual error estimates propagated from DoPHOT for weighting. Table 2 lists the coefficients from the solution for the night of 2007 October 12, as an example of the values and the residuals. Figure 4 shows residuals from the same night plotted against both airmass and color of the star. The rms scatter is less than 0.02 mag, typical of nights that were a posteriori considered photometric. Nights when any of the four passbands show rms scatter exceeding 0.03 mag were discarded, since conditions may be suspect.

Once the coefficients in Equation (3) were evaluated, and the fit residuals found to be satisfactory, the 0.9 m telescope instrumental magnitudes of the target object fields were transformed to true magnitudes on the system of Landolt or of Washington

Table 2
Example Photometric Solution (for 2007 October 12)

Passband	α	β	γ	COLOR	rms Residual	No. of Obs.
R	7.573	0.080	-0.014	$R - I$.018	136
R	7.576	0.081	-0.003	$C - R$.014	67
I	8.427	0.039	-0.018	$R - I$.020	130
C	8.021	0.312	-0.021	$C - R$	0.019	68
M	6.901	0.142	-0.015	$M - R$	0.020	66

(as appropriate for that band), by inverting Equation (3) and using the now known values for α , β , and γ .

3.6. Transfer of Calibrated Magnitudes to the MOSAIC2 Results

Transferring the calibration to the MOSAIC2 data involves several steps. First, the instrumental magnitudes from the deep, (medium,) and shallow images from MOSAIC2 for any passband are merged. Stars in common are recognized, and any offsets in instrumental magnitudes are adjusted. Such offsets can occur because of observations at different airmass, or due to throughput differences on different observing runs. For a given band, a single list is created, which contains objects from all the final images in that band. Where an object occurs on two or more of the lists, the weighted average is taken (weighted by inverse variance) using individual values for each star. The propagated error is also the weighted error derived from the component error values. The combined list for the R band serves as the master list, and the final lists from the other four bands for MOSAIC2 (C , I , M , and $DDO51$) are matched to the master list. A combined MOSAIC2 list is created, which now has an entry for each star detected in R , with instrumental magnitude and error values in each band for which a measurement is available. By construction, there is always a measurement available for R .

The instrumental magnitudes from any given image derived from MOSAIC2 observations are expected to differ from true magnitudes by a zero-point adjustment and a first-order color term. Atmospheric extinction suffered by the MOSAIC2 images is subsumed in these two terms. Accordingly, we can write (for example)

$$R = R' + \mathcal{A} + \mathcal{B}(R' - I'), \quad (4)$$

where R' and I' are instrumental mags for a given star from MOSAIC2, and R and I are the true values. The coefficients \mathcal{A} and \mathcal{B} can thus be derived. Any passband and instrumental color can be used in the form shown above, each with their respective coefficients. In practice, given that we use only those stars for which measurements exist in R , for any band X , where $X \neq R$, the instrumental color ($R' - X'$) is always available. For R itself, we solve for alternate colors: $R' - I'$, as well as $C' - R'$, which covers objects too blue to be detected in I , as well as those too red to be detected in C . Typical residuals for a fit to Equation (4) are shown in Figure 5. Once the coefficients are derived from the stars in common to MOSAIC2 and CFCCD, the values can be applied to all stars in the MOSAIC2 list for R , I , C , and M . These are the final calibrated magnitudes on the Landolt system for R and I , and on the Washington systems for C and M .

Since $DDO51$ magnitudes are not obtained with the CFCCD (it is unnecessary, and it would take too long an exposure to get sufficient numbers of stars to match against MOSAIC2), the $DDO51$ measurements at this point are uncalibrated. We force an artificial calibration using the precept that the metal absorption features in the $DDO51$ band do not form sufficiently

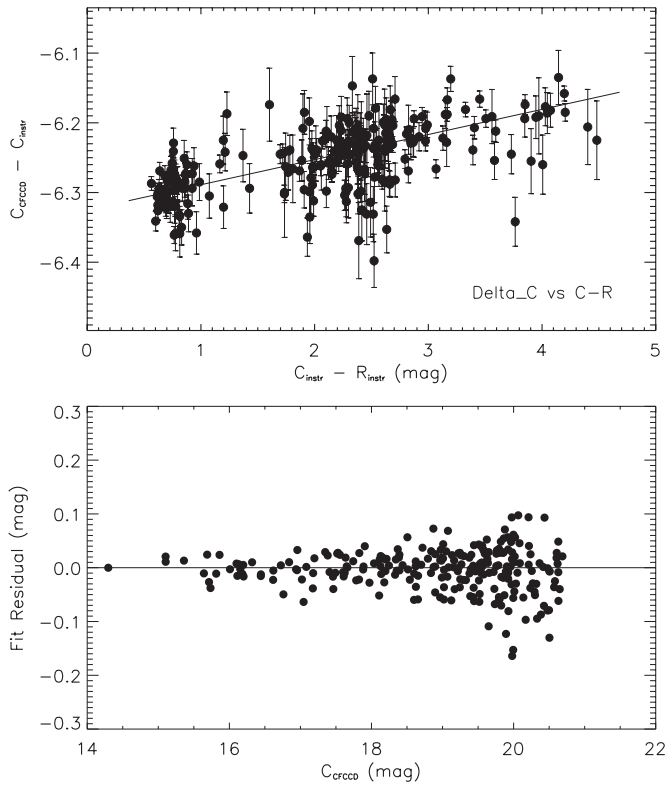


Figure 5. Illustration of the calibration of MOSAIC2 magnitudes as described in Section 3.6. The upper panel shows the color-dependent mapping from instrumental magnitudes in the C band measured with MOSAIC2 (denoted by C_{instr}) against C magnitudes on the Washington system established for CFCCD observations (denoted by C_{CFCCD}) as described in Section 3.5. The lower panel shows the fits residuals as a function of true C magnitudes. This example shown is for the field F601. The rms scatter in the fit, which includes objects spanning 6 mag in brightness, is 0.039 mag, with a weighted uncertainty in the mean of only 0.0023 mag.

in stars that are hot, or more specifically, that differences in relative transmission through the $DDO51$ and M passbands for such stars are not significant. Since the $DDO51$ passband lies in the middle of the M passband, we force the $DDO51$ band to equal the M -band mag on average, for all definite stars brighter than $I = 20.0$ with estimated measurement errors in the M and $DDO51$ bands less than 0.05 mag and estimated I error less than 0.1 mag that have $M - I < 1.0$. We denote this ersatz $DDO51$ magnitude value by $DDO51s$ (though we continue to refer to the passband by $DDO51$).

3.6.1. Consequence of Not Using Independent Color Terms for each CCD

The procedure above makes the tacit assumption that the color responses of the eight CCDs of MOSAIC2 are identical, so that a single pair of coefficients \mathcal{A} and \mathcal{B} can be used in Equation (4). While the flat-field normalization does a zeroth-order balancing of the responses, color terms remain because the color of the flat field is not the same as the color of a star, and stars themselves span a large range of colors. The overlap of the two CFCCD pointings over each MOSAIC2 field allows for common stars to be found on all eight CCDs of MOSAIC2, so in principle one can solve for eight different values of \mathcal{A} and \mathcal{B} , one pair for each CCD. The procedure would thus be quite straightforward, but would *require* that observations exist with both pointings of the CFCCD. Also, in the fields with higher Galactic latitude, the number of high S/N stars measured in the overlap area with any

one MOSAIC2 chip can get quite small, thus incurring larger uncertainties due to random errors of measurement. Another strategy could be to document the color response difference for each chip with respect to the mean obtained from comparing four or eight of the CCDs together.

To evaluate the chip-to-chip variations, on a photometric night (otherwise unusable because of poor seeing) we obtained observations of a standard field, placing the same stars in turn on all eight MOSAIC2 CCDs. Using the R band as an example, and using all available measurements on all chips, we first estimate the effects of extinction to zeroth order and solve Equation (3). This forces an initial solution assuming no color dependence variations from one CCD to another. We retain the value of β (airmass dependence) from this solution. Next, we force the above derived values of β and construct the extinction independent (to first order) instrumental mags for the R , I , and C bands as follows:

$$R'' = R' - \beta_R X, \quad (5)$$

$$I'' = I' - \beta_I X, \quad (6)$$

$$C'' = C' - \beta_C X. \quad (7)$$

Using these airmass dependence corrected instrumental mags, we then solve the following equations *independently* for each CCD:

$$R = R'' + \mathcal{A}'_R + \mathcal{B}'_R \cdot (R'' - I''), \quad (8)$$

$$I = I'' + \mathcal{A}'_I + \mathcal{B}'_I \cdot (R'' - I''), \quad (9)$$

$$C = C'' + \mathcal{A}'_C + \mathcal{B}'_C \cdot (C'' - R''). \quad (10)$$

Table 3 shows the values of \mathcal{A}' 's and \mathcal{B}' 's for each of the three above passbands for each of the eight CCDs, as measured on the night of 2005 October 3 (UT). The field contains six Landolt standards in SA 92: star numbers 245, 248, 249, 250, 252 and 253. These stars span a color range in $B - V$ from 0.5 to 1.4, which covers the color range of interest for this survey. Obviously, objects outside this range are interesting, but photometric accuracy demands for the analysis of ages and metallicities from Hess diagrams are well covered by this color range. Table 3 shows that within this color range, the rms scatter in recovering the standard star photometry is between 0.01 and 0.02 mag when analysis is done independently within each CCD. If a common solution is used with stars in all CCDs, the scatter increases marginally to about 0.02 mag. These results are also consistent with independent analysis in the C , M , $T1$, and $T2$ bands by one of us (K. Olsen 2009, private communication) using separate and independent data contemporaneous with this survey. We estimate, using the data in Table 3, that at $B - V = 0.0$, we could make a systematic error in color by at most 0.02, 0.03, and 0.04 mag in R , I , and C respectively, by ignoring color response variations from chip to chip. At $B - V = 1.5$, the errors can be as large as 0.04, 0.05, and 0.04 mag in R , I , and C , respectively. These are extreme cases, and as shown above, for the issues we seek to address, the rms errors incurred of 0.01–0.02 mag are no larger than other sources of error. We have therefore chosen the robustness of a single color term and zero point for all chips, over the difficulty of accurately pinning down the exact color terms, since the scientific return for doing so would be marginal at best.

Table 3
Chip-to-chip Response Variations in MOSAIC2 on 2005 October 3 (UT)

Passband	CCD Chip No.	A'	B'	rms Residual	No. of Stars Used
<i>R</i>	1	-4.276	0.076	0.011	6
	2	-4.297	0.045	0.012	6
	3	-4.320	0.039	0.012	6
	4	-4.289	0.078	0.012	6
	5	-4.292	0.019	0.010	6
	6	-4.297	0.016	0.011	6
	7	-4.298	0.019	0.013	6
	8	-4.295	0.012	0.013	6
	(All CCDs)	-4.296	0.038	0.017	48
<i>I</i>	1	-4.997	-0.028	0.020	6
	2	-5.001	-0.011	0.017	6
	3	-5.043	-0.022	0.015	6
	4	-5.003	-0.029	0.018	6
	5	-5.008	-0.096	0.018	6
	6	-5.012	-0.069	0.020	6
	7	-5.015	-0.066	0.018	6
	8	-5.016	-0.063	0.016	6
	(All CCDs)	-5.012	-0.047	0.022	48
<i>C</i>	1	-5.168	0.044	0.011	6
	2	-5.204	0.040	0.008	6
	3	-5.158	0.034	0.011	6
	4	-5.196	0.047	0.009	6
	5	-5.132	0.028	0.020	6
	6	-5.125	0.025	0.013	6
	7	-5.218	0.043	0.006	6
	8	-5.200	0.038	0.010	6
	(All CCDs)	-5.165	0.037	0.022	48

4. COLOR–MAGNITUDE DIAGRAMS OF FIELDS ALONG A NORTHERN EXTENSION FROM THE LMC

In this paper, we present the photometry for fields along a line going due north from the LMC bar. These eight fields (Table 1) are F7N, F9N, F11N, F12p5N, F14N, F123N, F122N, and F121N.¹⁷ Their respective distances from the LMC center (on the sky) range from 7° to 19° . They all lie at a Galactic latitude $b \approx -34^\circ$. Their individual distances from the LMC center are listed in Table 4. In addition, we consider the two fields F111 and F113, which flank the line traced by the above fields at LMC-centric distances between 12° and 14° , which is where we originally expected to see a pile up of tidal debris, based on the tidal radius estimate by Weinberg (2000) done before the new and improved proper motion of the LMC was known (although we should point out that his estimate does not demand the orbit).

4.1. Comparison with Isochrones

Photometry in *CRI* for the field F7N, which is the closest to the LMC center, is shown as two CMD's (one with $R-I$ as color, and the other with $C-R$ as color) in Figure 6. Only objects that are classified definitely to be stars are plotted, which means that features that extend a magnitude fainter are not shown because there is not adequate S/N for them to be unambiguously distinguished as stars or as background compact galaxies. The CMDs show a well-defined giant branch and red clump/horizontal branch. The turnoff stars span a range of brightness: from about $I \sim 21.0$ at the faint end to those still on the MS extending as bright as $I \sim 18$.

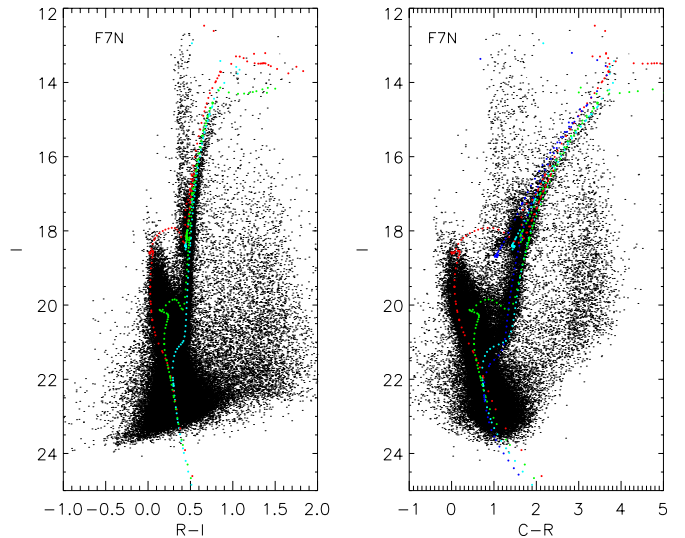


Figure 6. CMDs of the F7N field are shown: the left panel shows $R-I$ vs. I , and the right panel shows $C-R$ vs. I . Only objects whose PSF profiles are unambiguously consistent with those of a stellar PSF are shown. Several isochrones from Marigo et al. (2008) are overplotted, assuming a distance modulus of 18.55, and reddening $E(B-V) = 0.05$: the isochrone in dark blue is for $Z = 0.001$ and $\log t = 10.15$, the light blue is for $Z = 0.002$ and $\log t = 9.9$, the green if for $Z = 0.004$ and $\log t = 9.3$, and red for $Z = 0.008$ and $\log t = 8.7$. These are not rigorous fits to the data, but serve to illustrate the range of ages present, and that progressively younger stars are also progressively metal rich. We also note the foreground wall of disk, thick disk and halo turnoff stars at $R-I \sim 0.25$ and the pile-up of cool stars at $C-R \sim 3$.

Select isochrones from Marigo et al. (2008)¹⁸ are overplotted in Figure 6, and annotated in the figure caption. These tracks are “fit” by eye and are no substitute for a rigorous analysis of the Hess diagram, which will be the subject of a future paper. However, even the relatively rudimentary exercise of producing these figures has been revealing. The “fits” are constrained by having to accommodate the width of the MS, the width of the sub-giant branch (SGB), and the colors of the brighter RGB. The dark blue isochrone (shown only in the right-hand panel of Figure 6) shows that 14 Gyr metal poor stars are rare, for neither the SGB nor the upper RGB are fit by this isochrone. But there must be some stars, perhaps 10 Gyr or older, to explain the blue extension of the red clump into a horizontal branch, as seen in the $C-R$ versus I CMD. It is not possible to measure the star formation rates without a full quantitative Hess diagram analysis (planned in the near future) but the isochrone fits indicate that stars older than 8 Gyr are rare. Uncertainties of order 0.1 mag in the distance modulus, or 0.05 mag in $E(B-V)$ reddening affect the finer details, but not the overall conclusions. The isochrones “allowed” by the CMD constrain what age–metal combinations are permissible: the oldest stars have $Z \sim 0.001$, and the youngest about $Z \sim 0.008$. This corroborates the finding by Gallart et al. (2008) in their study of fields from $2:3$ to $7:1$ from the center of the LMC, that younger stars must be progressively metal-rich.

Predictably enough, it is the CMD in $C-R$ which primarily drives and constrains the isochrone comparisons and demands that metals increase for younger stars. This justifies adding the observationally expensive C band data, which allows purchase on the metallicity. Changing the metallicity by a factor of two at a given age quite dramatically degrades agreement of the data with an isochrone; changing age by 20% at fixed metallicity

¹⁷ The combined images and calibrated photometry for these fields are being made available in the NOAO survey program archives.

¹⁸ Obtained from <http://stev.oapd.inaf.it/cgi-bin/cmd>.

Table 4
Numbers of Stars in Selected CMD Regions in the LMC Extension Fields

Field Name	Distance from LMC Center (degrees on sky)	No. in MS Region	No. in RGB Region	No. of D51s Selected Giants
(1)	(2)	(3)	(4)	(5)
F7N	7.0	23409	532	463
F9N	9.0	4462	109	54
F11N	11.0	1119	55	4
F12p5N	12.5	537	55	2
F14N	14.0	281	47	11
F123	16.0	91	45	2
F122	17.5	72	49	3
F121	19.0	71	38	5
C18	34.0	78	63	9
F111	14.0	267	52	9
F113	12.7	308	65	16

also does the same. It is additionally satisfying that the chosen isochrones cover *both* CMDs, i.e., in $R - I$ as well as in $C - R$, which lends confidence and credibility to the outcome. A future detailed Hess diagram analysis will bring to bear all of the constraints on ages and metallicities inherent in the C , M , R , I bands, to provide a well-constrained star formation history.

The CMDs in $C - R$ versus I are shown for the fields with progressively increasing distances in Figures 7 and 8. The isochrone for $Z = 0.002$ and $\log t = 9.9$ (8 Gyr) at a distance modulus of 18.55 and reddened by $E(B - V) = 0.05$ is overplotted on all eight CMDs. The CMDs from the flanking fields F111, F113 are shown in Figure 9.

A smooth progression in the features of the CMD is apparent. Going from 7° through 9° to 11° , we see not only a decline in the total number of stars present, but also a steady erosion of the younger stars relative to the older ones, as seen from the sharp decline in the number of blue MS stars (above the oldest turnoff). By the time we are 11° out, the young stars are all essentially gone. The overall decline in the number of all stars also causes the RGB to vanish against the “backdrop” of foreground stars from the Galaxy: it is clearly delineated in F7N, still quite visible in F9N, but not discernible on its own in the CMD of F11N. In contrast, the MS stars clearly continue to stand out prominently.

This is the expected validation of one of the basic precepts of this survey: that of reaching the MS stars below the oldest turnoff, and using them as tracers of extended structure. Anticipating the counts of stars in the MS described later in this section, we derive the equivalent surface brightness in I from the stars in the MS at the location of F11N to be ~ 30.5 mag arcsec $^{-2}$. This is several hundred times fainter than the sky brightness. Surface brightness measurements in galaxies farther away would not reveal the equivalent structure, and as evidenced here, RGB stars are too sparse (nearly 100 times sparser than the MS stars) to be useful for tracing kiloparsec scale structure. However, the MS stars allow us to push on. Proceeding through the CMDs of fields even farther out (see Figure 8), the MS feature persists through the field at 14° (F14N) and is visible even in the 16° field (F123). In the two outermost fields (F122 at $17^\circ.5$ and F121 at 19°), the last vestiges of the MS disappear into the ambient stars in the line of sight. In F14N, the equivalent surface brightness in I of the MS stars is ~ 32.3 , and in F123 it is ~ 34.8 mag arcsec $^{-2}$. Real-surface brightness detections of structure in any galaxy at such levels is not possible with any foreseeable instrumentation, whether from the ground, or from space, since these are 10^4 times or more fainter than the ambient sky brightness. If the

LMC were twice as far away than it is, the MS even in the F11N field would disappear into the cloud of unresolved galaxies for ground-based observations, though it would remain accessible to space based imaging. The LMC (and the SMC) thus provides us with an unprecedented opportunity to probe structure that is bound to a parent galaxy, using MS star counts.

4.2. Identifying Giants Using the DDO51 Photometry

The DDO51 passband, originally defined by Clark & McClure (1979), and introduced into the Washington system by Geisler (1984), admits a narrow (~ 100 Å wide) part of the spectrum centered near 5150 Å, and includes the Mg I triplet and bands of MgH, which are sensitive to surface gravity (in addition to temperature and abundance). These spectral features have been widely used to separate G and K giants from dwarfs in the same temperature range from low dispersion spectra. The DDO51 passband is able to do the same from appropriate photometric data. The strength of the absorption features is measured by the index $M - DDO51s$, since DDO51 is conveniently situated in the middle of the M passband. A second index must be used to track and de-trend the effects of temperature. Details on implementing this technique are given by Majewski et al. (2000). They used $M - T2$ (Washington system) as the temperature index. Their Figure 4 demonstrates the sensitivity of the method for stars with colors redward of the turnoff for old stars.

An elaborate critical discussion of this technique, replete with caveats and limitations, is given in Morrison et al. (2001). Specifically they warn that errors in both $M - T2$ and $M - DDO51$ need to be held within a few hundredths of a magnitude to avoid specious detections of giants because of photometric error driven contamination from the much more numerous MS stars.

Our implementation has a couple of subtle differences from that of both Majewski et al. (2000) and Morrison et al. (2001). We choose $M - I$ as the temperature index, noting that I is very close to the $T2$ band. Also, instead of DDO51 magnitudes defined by Geisler (1984), we use DDO51s, as defined in Section 3.6. We define our procedure empirically, using the photometric data for the field F7N, where the giants are numerous and easily seen in the CMDs.

Consider Figure 10. The left panel shows the color-color diagram of $M - DDO51s$ versus $M - I$ for stars brighter than $I = 18$ (LMC giants brighter than the red clump cannot be fainter than this), and where the reported uncertainties for M , I , and DDO51s are all less than 0.03 mag. At blue colors, or $M - I < 1.0$, all stars merge to $M - DDO51s \sim 0.0$, by construction.

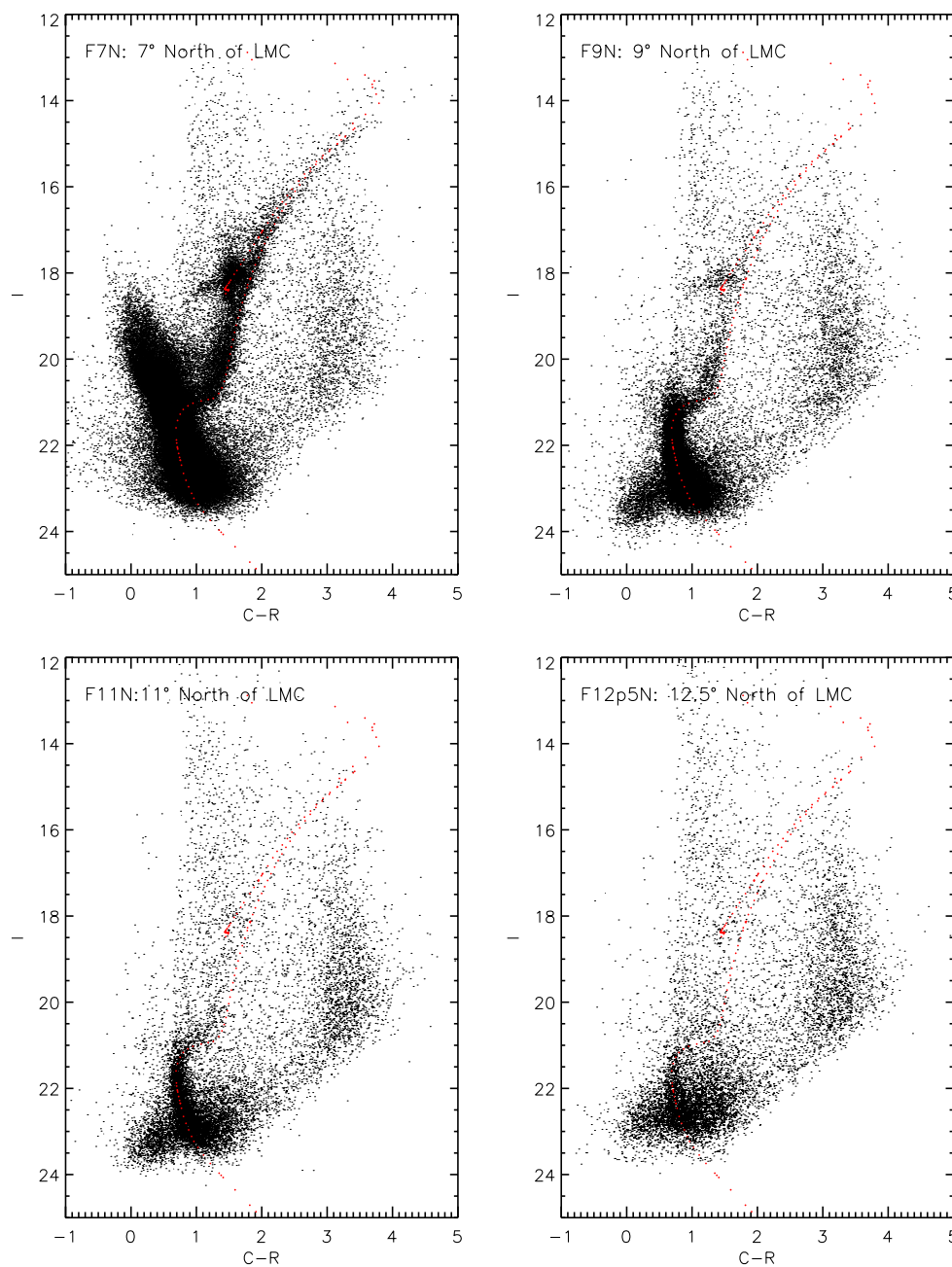


Figure 7. CMDs in $C - R$ vs. I are shown for fields progressively more distant (from 7° to 12.5°) along a line due north from the center of the LMC. All objects whose profiles are consistent with those of a stellar PSF are shown. The majority of objects fainter than $I = 22.5$ and with colors ranging from $0 < C - R < 1.5$, especially in the more distant fields, are background galaxies, unresolved in the seeing limited images. The isochrone for $Z = 0.002$ and $\log t = 9.9$ (8 Gyr) is overplotted. See Section 4.1 for interpretation.

At redder colors, especially going past $M - I \sim 1.2$, we see separation into two branches. The lower branch is populated by the foreground dwarfs, and the upper branch corresponds to giants. For very much redder colors, $M - I > 3.0$ the two branches merge again, and dwarf versus giant separation fails with this method at very low temperatures. Stars enclosed in the indicated region bounded in red are designed to include giants and reject dwarfs.

The right-hand panel of Figure 10 shows the now familiar CMD with I versus $C - R$. The points shown in green are the same stars that enclosed in the “giants” area on the left-hand panel. They lie on the giant branch location for the LMC giants thereby demonstrating the efficacy of the method. There are a few stars that follow the shape of the LMC giant branch, but lie

above the visible concentration of RGB stars: these may be AGB stars, or perhaps they indicate the presence of complex structure in the RGB, possibly arising from the significant range of ages and metallicities indicated by the complex mixture evident from the MSTO region. A third possibility is that some of these stars are from the Galaxy halo: we defer discussion of this to Section 5.

It is notable that not all stars along the giant branch locus are marked in green. Some of the unmarked ones are doubtless because they are really foreground dwarfs that happen to lie along that locus. Note that there are several unmarked stars near $C - R \sim 2.0 \pm 0.2$ and $I \sim 17.3$, where the density of points indicates that many of these must be LMC giants. Thus in this example we may have erred on the side of not

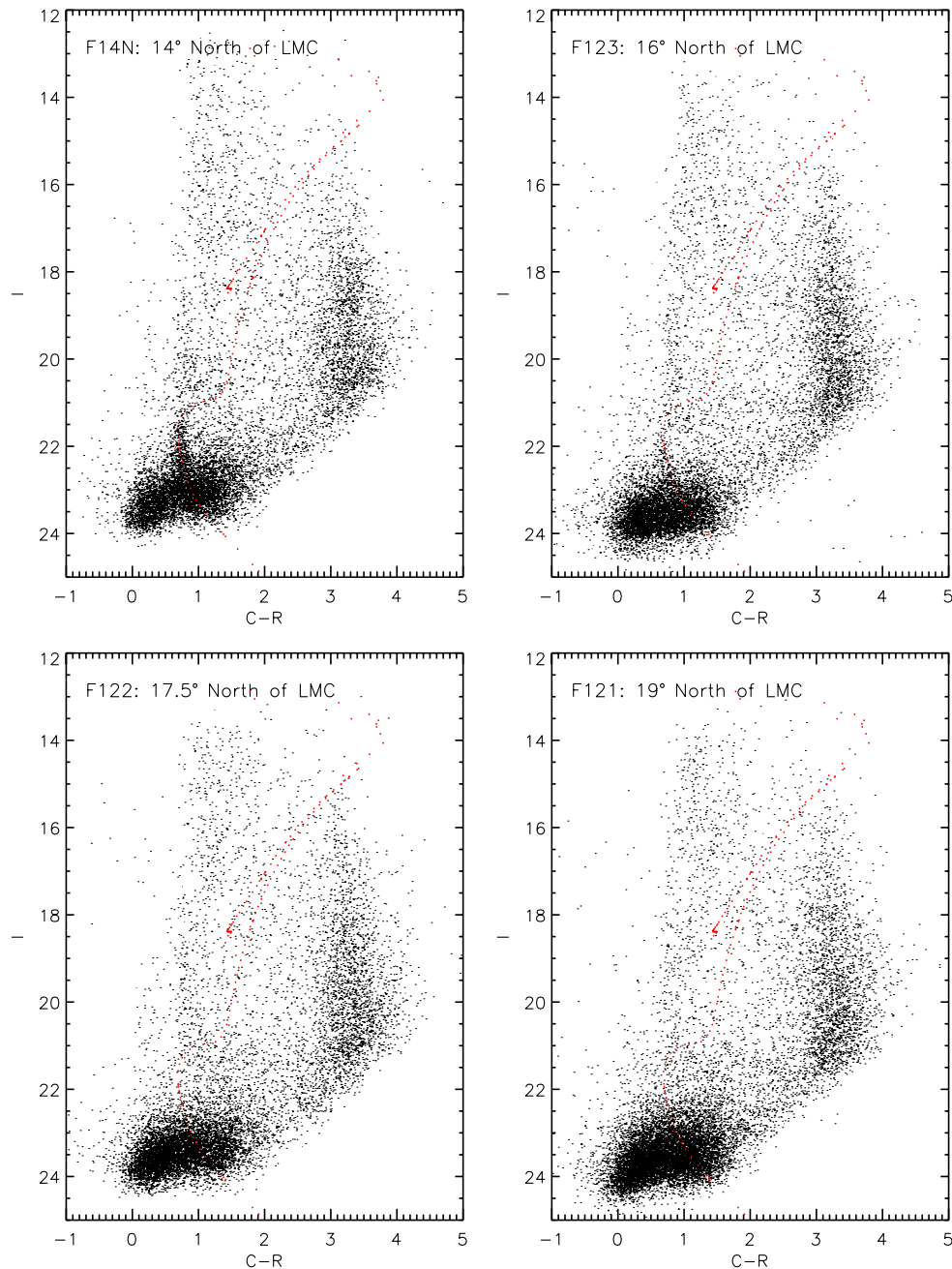


Figure 8. Same as Figure 7, but for fields at distances from 14° to 19° from the LMC center.

including bona fide giants. Had we widened the enclosed area on the left-hand color-color diagram, we might have included more giants, but at some point we would also begin to include non-giants. The point is that this method can be used to identify giant candidates, which must later be followed up spectroscopically for confirmation. We should be circumspect about using this method to count giants, because how we set our color-color limits, and the accuracy of photometry will govern the completeness as well as pollution of our giant sample. As a pre-selection of objects for follow up spectroscopy, this method is excellent, but one should be wary of making a stellar census from giants selected in this way.

Figure 11 shows the reverse case, where a region of giants is chosen (very conservatively) on the CMD (shown in red on the right panel), and traced to the color-color diagram (left panel) where they are marked as green points (again, all points

shown have reported photometric errors less than 0.03 mag in I , M , and $DDO51s$). While the majority of the points fall on the “giant branch” of the color-color diagram, a significant number though are clearly dwarfs, since the CMD region also has stars from the Galaxy foreground that are dwarfs. In fields where the contribution from the LMC gets sparser, the marked region on the CMD will pick up more foreground dwarfs than LMC giants. Here also, one must independently assess the contribution of dwarfs in the RGB region from control fields at similar Galactic latitudes.

5. ANALYSIS OF STAR COUNTS

Figure 12 shows the CMD of the field F9N again, but with two regions marked. The lower region encloses part of the lower MS and the turnoff of the oldest stars. Its lowest (faintest) extremities are chosen to be such that even in the worst seeing

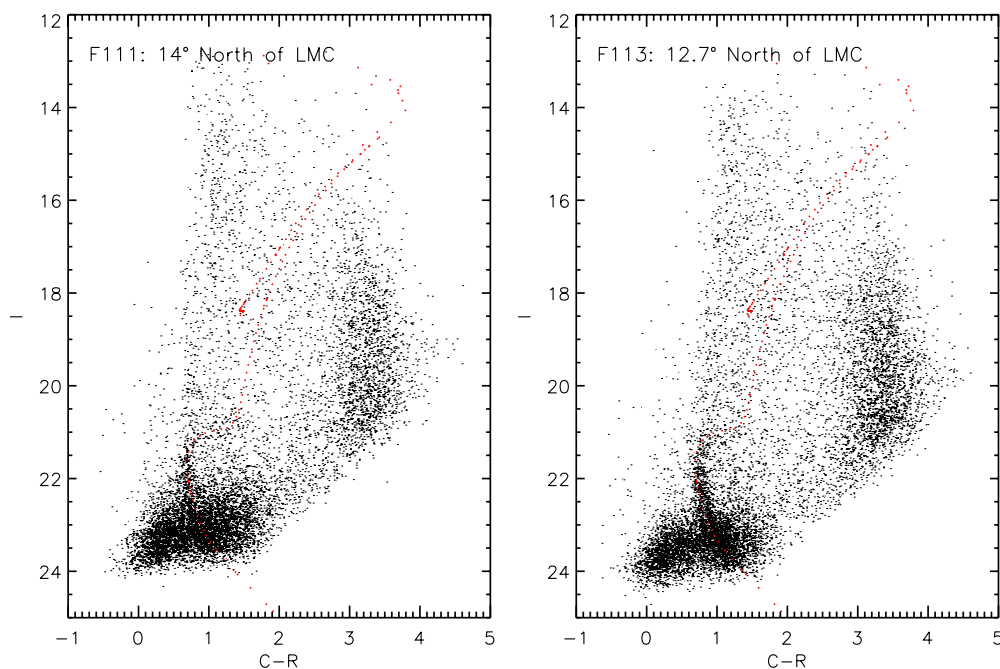


Figure 9. Same as Figure 7, but for the flanking fields between 12° and 14° from the LMC center.

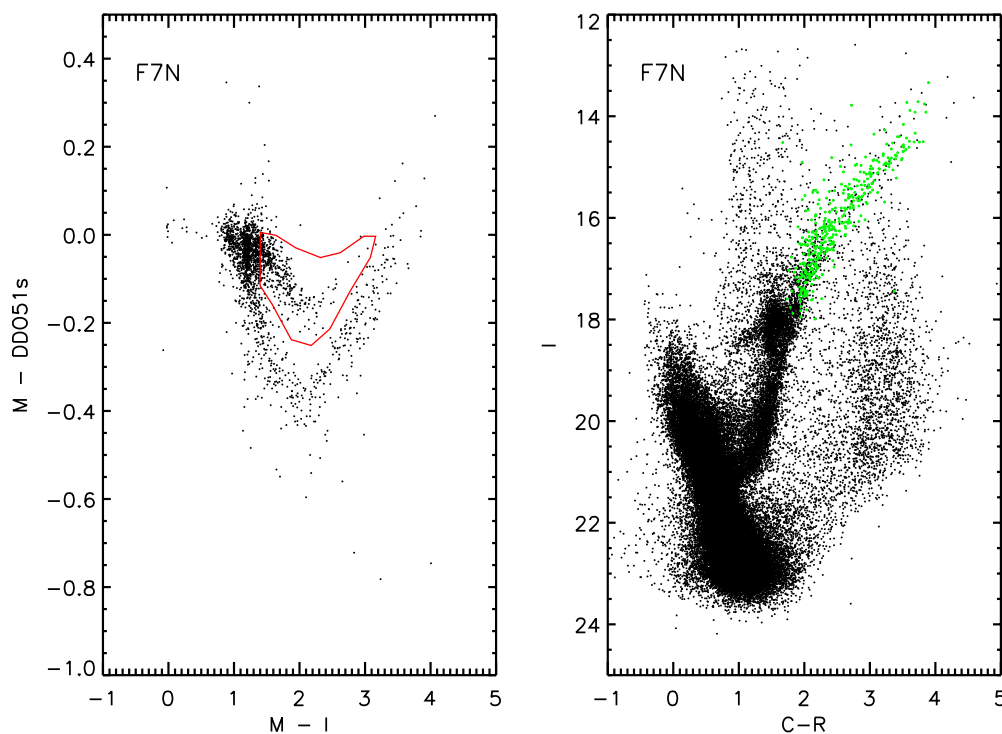


Figure 10. Left panel shows a color-color diagram, $M - DDO51s$ vs. $M - I$ for stars brighter than $I = 18.0$. The stars in the enclosed region are identified as candidate giants. On the right hand panel, these candidate giants are shown in green on the CMD in I vs. $C - R$. All of the objects fall in the region of the CMD containing the giants, demonstrating that this is a good and efficient way to identify giant candidates. See Section 4.2 for qualifications and caveats for this method.

images in any of the fields, the object detection is complete, and brighter than the cloud of potentially unresolved galaxies mentioned above. The higher region encloses the RGB stars brighter than the red clump (its definition really comes from the CMD of F7N, where the RGB is very clear). These regions have been defined so that the numbers of stars that lie within their boundaries can be counted and compared across all the fields.

The control field C18 (see Table 1) is nominally a perfect reference for estimating contamination for all of these fields from

foreground stars from the Galaxy, as well as for background objects. However, this particular control field is itself contaminated: we were surprised to find that it contains stars that are an extension of the globular cluster NGC 1851, even though the field lies several tidal radii from the cluster. This in itself was an exciting discovery and is reported elsewhere (Olszewski et al. 2009) including a follow up investigation. If we discard C18 as a result of the above anomaly, we can use F121 and F122 as control fields a posteriori, since they show no presence of stars associated with the LMC.

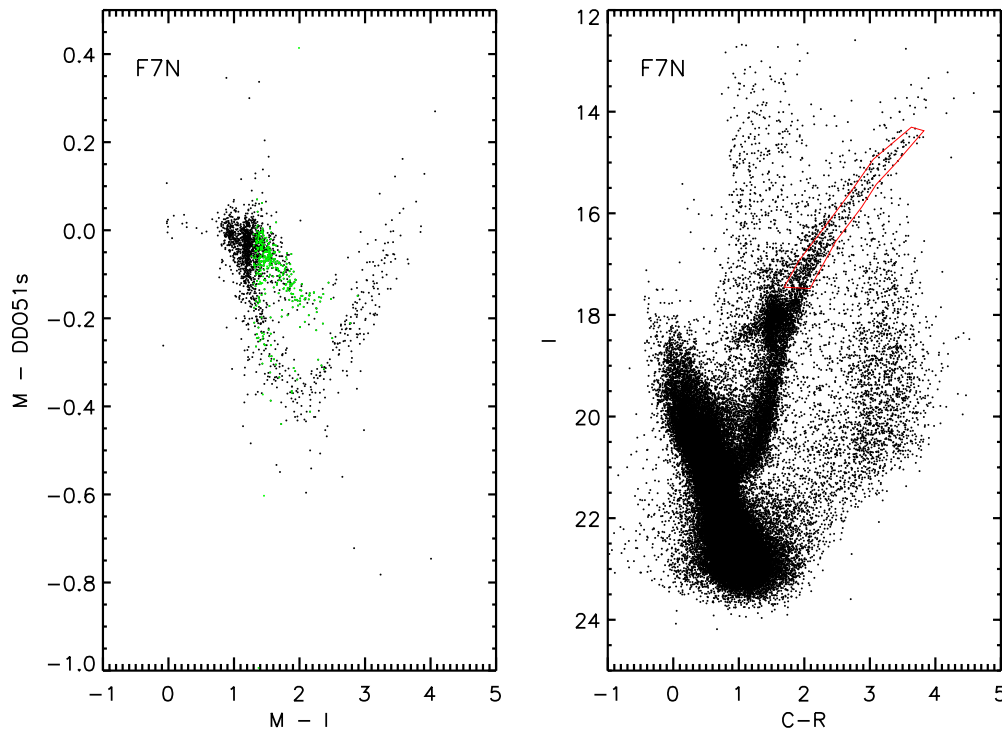


Figure 11. Same as Figure 10, but here the stars in the right-hand panel enclosed in the RGB region are mapped onto the color-color diagram in the left panel and shown as green points. While the majority of the points fall on the “giant branch” of the color-color diagram, a significant number though are clearly dwarfs, since the CMD region also has stars from the Galaxy foreground that are dwarfs. See Section 4.2 for a fuller discussion.

It turns out, fortuitously, that while stars associated with NGC 1851 are clearly present in the CMD of C18, they do *not* visibly pollute the two regions defined here. Figure 13 shows the I versus $C-R$ CMD for the field C18. The feature corresponding to the MS of NGC 1851 is clearly visible. An isochrone ($Z = 0.001$ and $\log t = 10.1$) from Marigo et al. (2008) is overplotted, using $E(B - V) = 0.02$ and $m - M = 15.2$, which matches the visible MS. Also overplotted are the MS and RGB regions corresponding to the LMC CMD: it is clear that both these regions should be free from stars associated with NGC 1851 and are therefore useful for estimating the residual star density in these CMD regions. We thus proceed with caution to see if star counts from C18 can also help with background estimation.

The counts of stars in the two regions defined above for the various fields being considered are presented in Table 4. In addition, the number of giants identified by the color-color diagram of $M - D51s$ versus $M - I$ described in Section 4.2 are listed in Column 4. The three farthest fields (F121, F122, and C18) show an average of 73 stars in the MS region, with scatter within Poisson statistics. Similarly, the number of stars in the RGB region averages to 50 for these three control regions, again within reasonable Poisson statistical bounds. It is immediately clear that with the exception of F7N and F9N, there are no significant excesses in the counts of RGB stars when compared to the control value, confirming our visual examination based inference that RGB stars run out as good tracers at distances larger than 8° or 9° . In comparison, the counts of MS stars (obtained by subtracting the average counts of stars in the MS locus on the CMDs for the three control fields) in our pre-defined region can be traced out as far as 16° (F123), with statistical significance, again corroborating our visual examination based inference.

Figure 14 shows the log of the surface density of stars in the MS region from Table 4 (after subtracting the average

background value from the three control fields, following the discussion above) against the projected distance from the LMC center. The excellent fit to an exponential decline in surface density over the entire range where MS stars associated with the LMC can be detected formally favors a pure disk, with a scale length of 1.32 on the sky. In Section 6.1, we show that de-projecting onto the plane of the LMC disk yields a disk scale length of 1.15 kpc. This value is remarkably close to that derived for the inner disk from counts of giants by van der Marel (2001), who obtained a scale length “ $r_d \approx 1.3-1.5$ kpc.” Other determinations of the interior disk scale length, $1.4-1.5$ kpc by Bothun & Thompson (1988), 1.42 kpc by Weinberg & Nikolaev (2001), and 1.47 kpc by Alves (2004) are all mutually consistent.

In comparison, Figure 15 which is a log-log plot of surface density versus distance from the LMC center, is unable to fit the full range simultaneously, and even where the decline is most gentle, implies a power law $\Sigma \propto R^{-6.85}$. In our own Galaxy, the halo has a much shallower radial dependence: Saha (1985) showed that out to Galactocentric distance of 25 kpc, the density of RR Lyrae stars is consistent with $\propto R^{-3}$. This analysis utilized additional data from Kinman et al. (1965), and also showed that the “halo” is an oblate spheroid near the Galaxy center, and becomes more spherical as one goes out from the center. Similarly, Zinn (1985) obtained a density distribution for globular clusters that is $\propto R^{-3.5}$. Since a spatial power law that is $\propto R^{-n}$ implies a surface density that is $\propto R^{1-n}$, these examples lead us to expect halo surface density gradients that have power law indices near -2 or -2.5 . The index implied above for the LMC extension is -6.85 which is very steep, and too far a departure from our expectation to be a convincing model for a spheroidal halo. In addition, given the remarkable agreement of the exponential disk scale length from our data with that from the prior value for the inner disk, in further discussion we exclude the possibility that we are seeing a spheroidal halo.

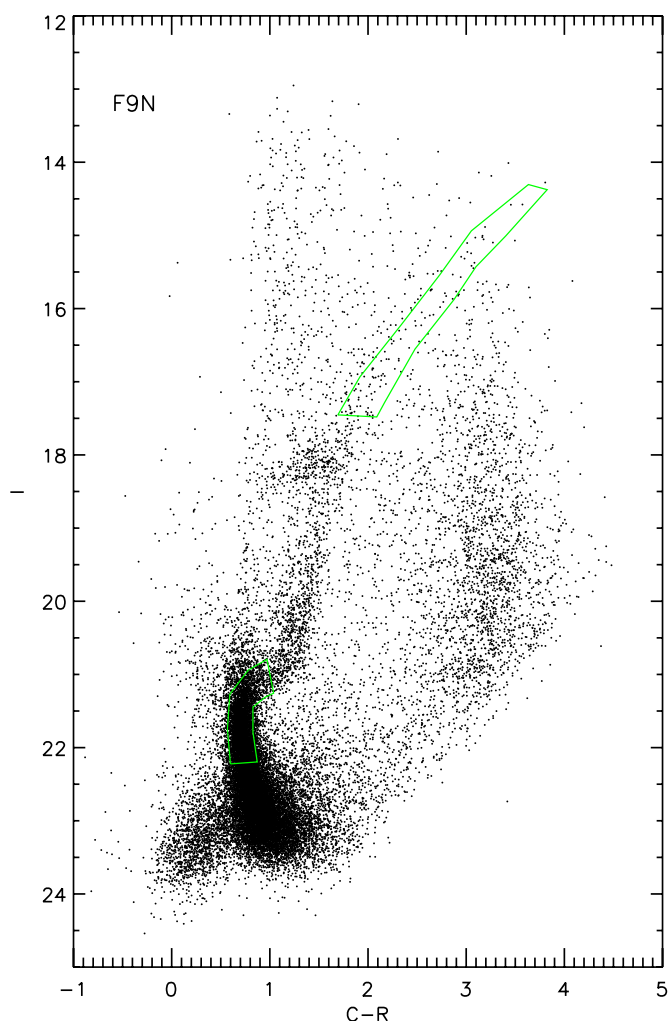


Figure 12. CMD of F9N is shown, on which two regions are marked. The lower one encloses stars with colors and brightness corresponding to the LMC MS and old turnoff. The upper region encloses the section of the CMD that contains RGB stars in the LMC brighter than the red clump: this region was actually traced from the CMD of F7N, where the RGB is better delineated.

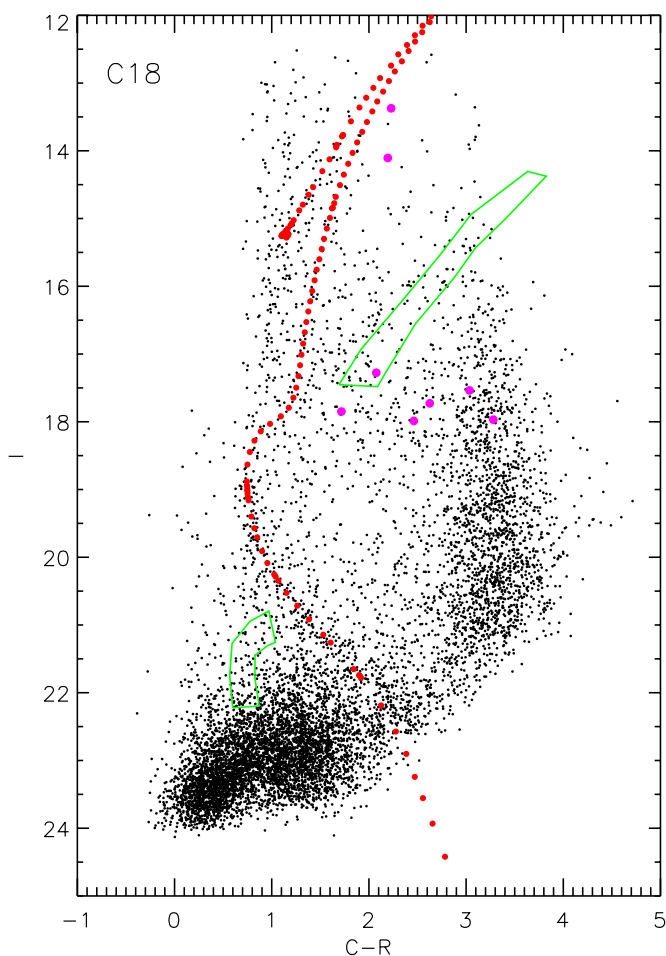


Figure 13. CMD of the field C18 is shown. This field is contaminated by the extended structure of the globular cluster NGC 1851: a locus of stars corresponding to the MS of this cluster is visible. An isochrone suitable for NGC 1851 is overplotted in red. The regions marked in green correspond to the LMC MS and LMC RGB stars, as for Figure 12. Note how both these regions should be clear of the isochrone, and hence not expected to be contaminated by stars belonging to NGC 1851. The stars picked up as potential RGB candidates are shown by the purple filled circles.

The average number of stars in the RGB region (Column 4 of Table 4) for the control fields F121, F122, and C18 is 50. The corresponding star counts in F11N through F14N and F123 are consistent with this value within 1σ Poisson errors. The formal average is one RGB star per field, or equivalently 3 deg^2 . Giants selected using the $D51s$ photometry (Column 5 in Table 4) also follow the same trend.

We have verified that all of the stars in F121 and F122 that lie inside the nominal RGB box in the $C - R$ versus I diagram, fall on the MS region of their respective $M - D51s$ versus $M - I$ diagrams. Thus they cannot be RGB stars. This also implies that the small positive number of putative giants found by the $D51s$ method are either specious, or not related to the LMC. The counts in Columns 4 and 5 of Table 4 for all fields except F7N, F9N, and C18 are similar enough to those in F121 and F122 within Poisson probabilities, that we can surmise that these fields are also free of LMC giants. Also note that when the “background” values are subtracted from the counts in Columns 4 and 5 (50 stars and 6 stars, respectively), the number of implied LMC giants is quite similar in both columns. Since each of these methods is afflicted in different ways (as discussed in Section 4.2) we find this rough agreement remarkable.

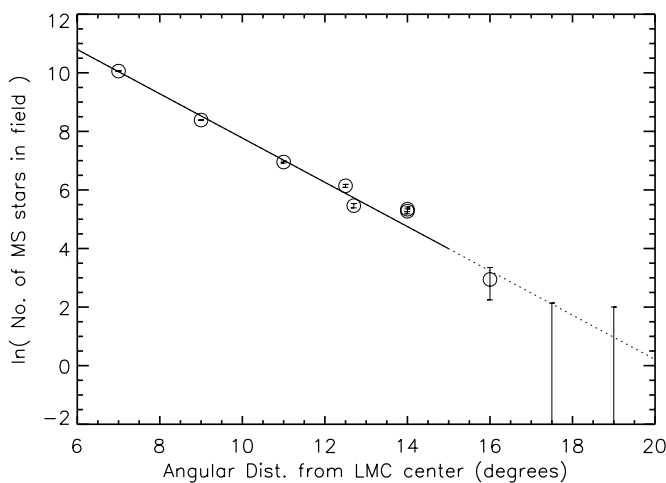


Figure 14. Run of the log of surface density of MS and old TO stars selected from a pre-defined region of the CMD (see Section 5 for details) with distance as projected on the sky along a direction due north from the LMC center. The line shown is a weighted fit to the inner eight points, which implies an exponential decrease in the surface density of these stars with distance, with a scale length of $1:32$ on the sky.

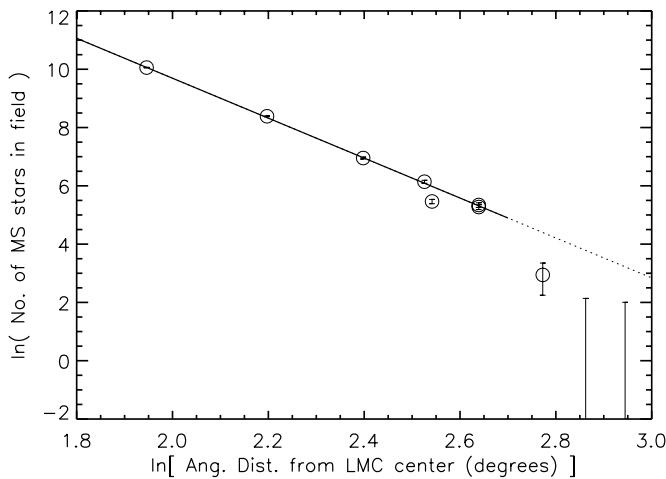


Figure 15. Same as Figure 14, but with the abscissa showing the log of the distance from the LMC center. A linear fit is possible only to the inner seven points, and the implied power law for surface density that results from such a weighted fit is $\Sigma \propto R^{-6.85}$. The unweighted fits is even steeper and implies $\Sigma \propto R^{-7.03}$.

In the fields F7N and F9N, the ratio of selected MS stars to RGB selected giants (after applying “background” corrections described above) is greater than 50 (formally 54 in F7N and 74 in F9N). We can thus assert that every bona fide giant in the LMC must be accompanied by at least 50 dwarfs in our MS counting region.

6. DISCUSSION

6.1. Further Characterization of the LMC Disk

Having established that we are tracing the continuation of the disk characterized by van der Marel (2001), it is important that we set our observations in that context, and on that system, especially to see where our fields lie on the plane of the LMC disk.

Whereas we used an LMC center with J2000 coordinates $\alpha = 5:23:34.0$ and $\delta = -69:45:00$ when designing our survey and calculating field positions, van der Marel (2001) uses a projection origin $\alpha = 5:29$ and $\delta = -69.5$. This results in a small change to the angular distances of each of our fields from the LMC center and are tabulated in Column 2 of Table 5. The line of sight along a given field intersects the LMC disk at a distance that is different from the distance to the LMC center, since the disk is tilted with the plane of the sky. These distances are calculated using the van der Marel disk geometry, and a fiducial distance to the LMC center of 50 kpc (which corresponds to a distance modulus of 18.50) and listed in Column 3 of Table 5. The corresponding distance modulus on the same basis is listed in Column 4. If the distance to the LMC center is denoted by D_0 , the line-of-sight distance to the disk by D , and if the angular distance of this line of sight from the LMC center is θ , then the distance ρ along the plane of the disk from the LMC center to the line-of-sight vector is given by

$$\rho^2 = D^2 + D_0^2 - 2DD_0 \cos(\theta). \quad (11)$$

Values of ρ for each of the fields used here in the investigation of LMC structure are listed in Column 5 of Table 5.

Figure 16 shows the run of surface density against true LMC-centric distance along van der Marel’s LMC disk. We have ignored any effects that disk warping and flaring would cause.

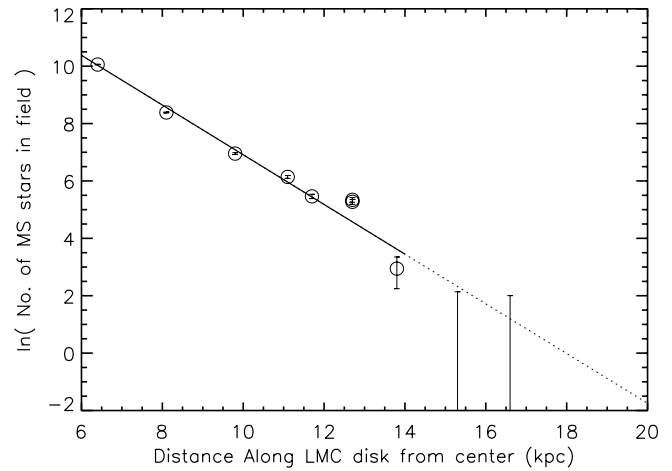


Figure 16. Same as Figure 14, but with the abscissa values showing distance along the plane of the LMC disk using the disk geometry from van der Marel (2001) and a fiducial distance to the LMC center of 50 kpc. A weighted linear fit to the inner eight points yields a disk scale length of 1.15 kpc and is shown by the line. An unweighted fit gives 1.20 kpc.

Table 5

Position of Fields with Respect to van der Marel’s LMC Disk Geometry

Field ID	Angular Distance from vdM Disk Center (degrees)	Line of Sight Distance (kpc)	$(m-M)$	Distance Along vdM LMC Plane (kpc)
(1)	(2)	(3)	(4)	(5)
F7N	6.77	47.3	18.37	6.4
F9N	8.77	46.6	18.34	8.1
F11N	10.77	46.0	18.31	9.8
F12p5N	12.26	45.6	18.30	11.1
F14N	14.18	45.2	18.27	12.7
F121	19.05	44.3	18.23	16.6
F122	17.43	44.6	18.25	15.3
F123	15.47	44.8	18.26	13.8
C18	28.84	43.9	18.21	24.1
F111	14.20	45.3	18.28	12.7
F113	12.65	44.7	18.25	11.7

Detection of such features in our data would require more complete spatial coverage.

6.2. Can There Be an Undetected LMC Halo?

We have shown that the LMC disk is traceable to 16° , which is more than 10 scale lengths. We must ascertain at what level our results rule out the existence of an LMC halo. We can first ask what one would see if a similar experiment were directed at the MW Galaxy, from a vantage point from which the plane of the Galaxy is seen face-on. We recognize that the literature provides a vast array of models for the MW disk, thick disk, halo, and bulge. Each is based on different tracers for these components, which in turn are normalized to all stars using IMFs and spatial dependences. Each approach has strong and weak points. A proper discussion of the state of knowledge is beyond the scope of this paper, but the interested reader can see, for example: Bahcall & Soneira (1985), Sandage & Fouts (1987), Sandage (1987), Morrison et al. (2000), and Robin et al. (2003). Instead we make a few heuristic assertions that we deem reasonable and proceed toward the goal of getting an approximate picture of the radial run of star count surface densities would look like if the Galaxy were viewed face on.

Accordingly we adopt from Drimmel & Spergel (2001) the MW radial disk scale length $r_{\text{GAL}} = 0.28 D_\odot$, where D_\odot is the

Galactocentric distance of the Sun. We assert that it is adequate for our purpose to assume that this applies to both the thin and thick disks. For the halo we adopt a simple spherical distribution with a power-law density dependence of $R^{-3.5}$, which is borne out by the density distribution of globular clusters (Zinn 1985) and consistent with the distribution of RR Lyrae stars (Saha 1985). This corresponds to a surface density distribution that is $\propto R^{-2.5}$. We query the Besancon model (Robin et al. 2003) for counts of stars with $3.5 \leq M_V \leq 6.0$ toward the north and south Galactic poles, segregated by thin disk, thick disk, halo, and bulge components, from which we can derive the approximate column densities of these stars. The luminosity cut is representative of the MS dwarfs that we have used to trace surface density in the LMC exterior. The counting of stars is done along a cylindrical column and not as seen in through an opening with a fixed solid angle. In this way, we derive a total column density of 3.56, 1.12, and 0.03 stars pc^{-2} for the thin disk, thick disk, and halo components, respectively, at D_\odot , and zero contribution from the bulge. These component column densities are identical to the surface densities from these components as seen by a hypothetical distant observer looking face-on at the Galaxy. We use these surface densities at the solar location in the Galaxy, we can invoke our simplistic disk–halo model, to obtain expressions for the run of disk and halo surface densities (Σ_{disk} and Σ_{halo} , respectively):

$$\Sigma_{\text{disk}} = 137.3e^{-D_\odot/0.28} \quad (12)$$

and

$$\Sigma_{\text{halo}} = 0.030 D_\odot^{-2.5}. \quad (13)$$

Figure 17 plots the relative contribution from disk and halo components as a function of distance along the disk. The disk continues to dominate till about 10 disk scale lengths. Thus, an observer looking face on at the MW would see a disk-like exponential fall off in star counts all the way to 10 scale lengths. While there is no reason at all to believe that the proportion of disk and halo should scale from one galaxy to another; nevertheless, this indicates that our non-detection of a halo in the LMC does not mean that it does not have one, since we know that the Galaxy does have a halo, but that it does not nominally become prominent until past 10 scale lengths (roughly 25 kpc). Of course other issues such as disk warping, and termination (tidal or otherwise) of either disk, or halo or both in the outer parts can complicate this simplistic scenario.

We can also compare the actual surface density values expected in a face-on viewing of the Galaxy with what we see in the LMC. In F11, we count about 1050 dwarfs belonging to the LMC (Table 4). The footprint of the MOSAIC2 field at the LMC distance is $\sim 0.25 \text{ kpc}^2$, thus implying a surface density of LMC dwarfs (picked from our CMD region) of $\sim 0.004 \text{ pc}^{-2}$. F11N is at about eight LMC disk scale lengths. The equivalent location of eight disk scale lengths in our Galaxy is at $\sim 2.3 D_\odot$, where the density of dwarfs with luminosity $3.5 \leq M_V \leq 6.0$ (i.e., commensurate with the dwarfs identified from our CMD region in the LMC) from the Galaxy disk is $\sim 0.04 \text{ pc}^{-2}$, with the halo contribution an order of magnitude or so lower.

A natural question to ask is what limits our data can place on the detection of an LMC halo yet farther out using the detection of RGB stars yet farther out (Nidever et al. 2007; Majewski et al. 1999, 2009). Our outermost detection of dwarfs is at 16° from the LMC in F123, with a dwarf surface density of ~ 20 per MOSAIC field, which translates to $8 \times 10^{-5} \text{ pc}^{-2}$. Let us, for the sake of argument, take the extreme position that at this location

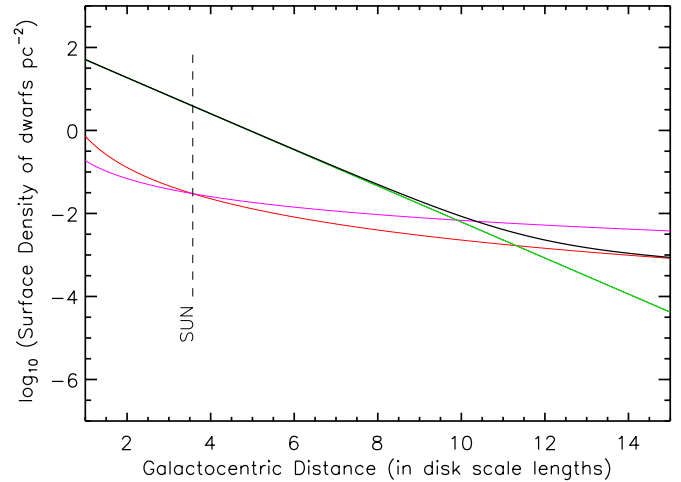


Figure 17. Run of surface star density for dwarfs in the luminosity range $3.5 \leq M_V \leq 6.0$, that would appear to an observer viewing the MW face-on from a large distance. The green line shows the contribution from the disk with scale length 0.28 times the Galactocentric distance of the Sun. Both thin and thick disk components are included. The red line shows the contribution from an $R^{-3.5}$ halo, whereas the magenta line shows the contribution if an $R^{-2.44}$ halo is assumed instead: they are normalized at the position of the Sun. The black line shows the combined contribution of stellar surface density of stars in the disk plus an $R^{-3.5}$ halo. For the details of the model, see Section 6. Irrespective of model differences, the overall conclusion is that in the MW, the halo does not overtake the disk till about 10 disk scale lengths, or about three times the Galactocentric distance of the Sun.

it is the halo, rather than the disk which is the main contributor, and further that the halo continues with a *flat* density out to the LMC distances reported by the above works. Their fields, which extend out to 23° from the LMC center, would have an upper limit for the surface count density of $8 \times 10^{-5} \text{ pc}^{-2}$. We have established in Section 5, that there must be at least 50 dwarfs for each RGB star seen, which therefore places an upper limit of $1.6 \times 10^{-6} \text{ pc}^{-2}$ or 1.6 kpc^{-2} for the column density of RGB stars, using our already extreme model for a putative LMC halo. This upper limit corresponds to one RGB star belonging to the LMC per square degree. An $R^{-3.5}$ halo instead of a flat continuation would imply one RGB star every 2.5 deg^2 at a field 23° from the LMC center.

Munoz et al. (2006) discovered a set of 15 giant stars roughly centered on Carina that have a velocity consistent with a smoothly changing LMC velocity and a velocity dispersion of 9.8 km s^{-1} . The density of these stars is $\sim 1 \text{ kpc}^{-2}$, which should be accompanied by ~ 25 dwarfs in our defined MS region per MOSAIC field. The distribution on the sky of these stars, discovered from a $4^\circ \times 4^\circ$ imaging survey is not smooth (see Figure 17 in Munoz et al.), and we speculate that it is consistent with stripping from the LMC disk itself.

An $R^{-3.5}$ halo that overtakes the disk at 16° from the LMC center predicts 16 dwarfs in our F122 field and 13 in the F121 field. We have found a total of 143 objects (from Table 4) in the MS region of the CMD (with no back/foreground correction) in these two fields taken together. For 29 of these to be LMC stars, the foreground–background counts in the MS region would have to be about 55 per field. We cannot altogether rule this out, but the fact that we see 78 total objects in the MS region for C18, which is 34° away, does not favor such a possibility. Besides the 20 dwarfs seen in F123 delineate a faint MS without difficulty, and so it is quite unlikely that 16 dwarfs in F122 would entirely escape being noticed by eye.

6.3. Summary

We have described our survey and the data processing. We have demonstrated in this paper that the data are of adequate quality for addressing the questions that have motivated this survey.

We have presented the results for a set of fields extending due north from the LMC, where we are able to trace stars associated with the LMC out past 10 disk scale lengths, which is unprecedented for any galaxy to date. This corresponds to surface brightness levels of 34 mag arcsec⁻².

The observed surface density of stars is consistent with a spatial distribution due to an exponential disk with scale length ≈ 1.15 kpc, which agrees with previous determination of the scale of the LMC disk interior to 9 kpc. We are unable to detect a contribution from a spheroidal halo component. Rather, we note that out along this direction due north from the LMC center, the structure of the disk appears perfectly disklike and unperturbed out to ~ 16 kpc. There are no noticeable effects from tidal stripping. Of course, this direction was chosen because by running parallel to the Galactic plane, and by being in the direction opposite to the SMC, it was expected to be the least affected by tides. Even so, our result is noteworthy, since this line of fields goes twice as far out from the LMC compared to the region where tidal streamers in H I and in carbon stars have been reported by Olsen & Massey (2007). It goes without saying that scrutiny of results from future analyses in other fields and regions of our survey will hold great interest.

In future papers, we will present both, similar analysis of data from other fields and detailed population analyses of Hess diagrams, in the various locations that we have sampled.

We thank the CTIO staff, especially the telescope operators and technical staff, for their help on the many observing runs. We also thank the NOAO archive group for making it easy to retrieve our data from the Tucson archive, and for their help with getting our final processed images ready for the public archive. A. Saha thanks Frank Valdes for illuminating discussions about image processing in general, and IRAF help in particular. E.O. acknowledges the NSF Grant AST-0807498. B.B. gratefully acknowledges fellowship support from the Indiana Space Grant Consortium. D.M. is supported by grants from FONDAP CFA 15010003, BASAL CATA PFB-06, and MIDEPLAN MWM P07-021-F. A.R. thanks the NOAO Goldberg Fellowship Program for its support.

REFERENCES

- Alves, D. R. 2004, *ApJ*, 601, L151
 Bahcall, J. N., & Soneira, R. M. 1984, *ApJS*, 55, 67
 Bothun, G. D., & Thompson, I. B. 1988, *AJ*, 96, 877
 Canterna, R. 1976, *AJ*, 81, 228
 Clark, J. P. A., & McClure, R. D. 1979, *PASP*, 91, 507
 Dolphin, A. E., Walker, A. R., Hodge, P. W., Mateo, M., Olszewski, E. W., Schommer, R. A., & Suntzeff, N. B. 2001, *ApJ*, 562, 303
 Drimmel, R., & Spergel, D. N. 2001, *ApJ*, 556, 181
 Feast, M. W. 1968, *MNRAS*, 140, 345
 Freeman, K. C., Illingworth, G., & Oemler, A., Jr. 1983, *ApJ*, 272, 488
 Gallart, C., Stetson, P. B., Hardy, E., Pont, F., & Zinn, R. 2004, *ApJ*, 614, L109
 Gallart, C., Stetson, P. B., Meschin, I. P., Pont, F., & Hardy, E. 2008, *ApJ*, 682, L89
 Geisler, D. 1984, *PASP*, 96, 723
 Geisler, D. 1996, *AJ*, 111, 480
 Harris, J. 2007, *ApJ*, 658, 345
 Irwin, M. 1991, in *IAU Symp.* 148, *The Magellanic Clouds*, ed. R. Haynes & D. Milne (Dordrecht: Kluwer), 453
 Kallivayalil, N., van der Marel, R. P., Alcock, C., Axelrod, T., Cook, K. H., Drake, A. J., & Geha, M. 2006, *ApJ*, 638, 772
 Kim, S., Staveley-Smith, L., Dopita, M. A., Sault, R. J., Freeman, K. C., Lee, Y., & Chu, Y. 2003, *ApJS*, 148, 473
 Kinman, T. D., Stryker, L. L., Hesser, J. E., Graham, J. A., Walker, A. R., Hazen, M. L., & Nemeč, J. M. 1991, *PASP*, 103, 1279
 Kinman, T. D., Wirtanen, C. A., & Janes, K. A. 1965, *ApJS*, 11, 223
 Kunkel, W. E., Irwin, M. J., & Demers, S. 1997, *A&AS*, 122, 463
 Landolt, A. 1983, *AJ*, 88, 439
 Landolt, A. 1992, *AJ*, 104, 340
 Majewski, S. R., Ostheimer, J. C., Kunkel, W. E., Johnston, K. V., Patterson, R. J., & Palma, C. 1999, in *IAU Symp.* 190, *New Views of the Magellanic Clouds*, ed. Y.-H. Chu et al. (San Francisco, CA: ASP), 508
 Majewski, S. R., Ostheimer, J. C., Kunkel, W. E., & Patterson, R. J. 2000, *AJ*, 120, 2550
 Majewski, S. R., Nidever, D. L., Muñoz, R. R., Patterson, R. J., Kunkel, W. E., & Carlin, J. L. 2009, in *IAU Symp.* 256, *The Magellanic System: Stars, Gas, and Galaxies*, ed. J. Th. van Loon & J. M. Oliveira (Cambridge: Cambridge Univ. Press), 51
 Majewski, S. R., Strzyski, M. F., Weinberg, M. D., & Ostheimer, J. C. 2003, *ApJ*, 599, 1082
 Marigo, P., Girardi, L., Bressan, A., Groenewegen, M. A. T., Silva, L., & Granato, G. L. 2008, *A&A*, 482, 883
 Massey, P., & Olsen, K. A. G. 2003, *AJ*, 126, 2867
 McClure-Griffiths, N. M., et al. 2009, *ApJS*, 181, 398
 Minniti, D., Borissova, J., Rejkuba, M., Alves, D. R., Cook, K. H., & Freeman, K. C. 2003, *Science*, 301, 1508
 Monet, D. G., et al. 2003, *AJ*, 125, 984
 Morrison, H. L., Mateo, M., Olszewski, E. W., Harding, P., Dohm-Palmer, R. C., Freeman, K. C., Norris, J., & Morita, M. 2000, *AJ*, 119, 2254
 Morrison, H. L., Olszewski, E. W., Mateo, M., Norris, J. E., Harding, P., Dohm-Palmer, R. C., & Freeman, K. C. 2001, *AJ*, 121, 283
 Munoz, R. R., et al. 2006, *ApJ*, 649, 201
 Nidever, D. L., Majewski, S. R., Munoz, R. R., Patterson, R. J., Kunkel, W. E., & Carlin, J. 2007, *BAAS*, 38, 942
 Olsen, K. A. G., & Massey, P. 2007, *ApJ*, 656, 61
 Olszewski, E., Saha, A., Knezek, P., Subramaniam, A., de Boer, T., & Seitzer, P. 2009, *AJ*, 138, 1570
 Piatek, S., Pryor, C., & Olszewski, E. W. 2008, *AJ*, 135, 1024
 Putman, M. E., et al. 1998, *Nature*, 394, 752
 Robin, A. C., Reyle, C., Derriere, S., & Picaud, S. 2003, *A&A*, 409, 523 (erratum: 416, 157 [2004])
 Saha, A. 1985, *ApJ*, 289, 310
 Sandage, A. 1987, *AJ*, 93, 610
 Sandage, A., & Fouts, G. 1987, *AJ*, 93, 592
 Schechter, P. L., Mateo, M., & Saha, A. 1993, *PASP*, 105, 1342
 Schlegel, D. J., Finkbeiner, D. P., & Davis, M. 1998, *ApJ*, 500, 525
 Schommer, R. A., Suntzeff, N. B., Olszewski, E. W., & Harris, H. C. 1992, *AJ*, 103, 447
 Stryker, L. L. 1984, *ApJS*, 55, 127
 Subramaniam, A., & Subramanian, S. 2009, *A&A*, 503, L9
 Suntzeff, N. B., Schommer, R. A., Olszewski, E. W., & Walker, A. R. 1992, *AJ*, 104, 1743
 van der Marel, R. P. 2001, *AJ*, 122, 1827
 van der Marel, R. P., Alves, D. R., Hardy, E., & Suntzeff, N. B. 2002, *AJ*, 124, 2639
 van der Marel, R. P., & Cioni, M. L. 2001, *AJ*, 122, 1807
 Weinberg, M. D. 2000, *ApJ*, 532, 922
 Weinberg, M. D., & Nikolaev, S. 2001, *ApJ*, 548, 712
 Zinn, R. 1985, *ApJ*, 293, 424